UNIVERSITY OF FRIBOURG (SWITZERLAND))

Sustaining cryosphere-fed irrigation networks with ice reservoirs

by

Suryanarayanan Balasubramanian

A thesis submitted in partial fulfillment for the degree of Doctor of Philosophy

in the
Faculty Name
Department of Geosciences

June 2022

Declaration of Authorship

I, Suryanarayanan Balasubramanian, declare that this thesis titled, 'Ice Reservoirs' and the work presented in it are my own. I confirm that:

- This work was done wholly or mainly while in candidature for a research degree at this University.
- Where any part of this thesis has previously been submitted for a degree or any other qualification at this University or any other institution, this has been clearly stated.
- Where I have consulted the published work of others, this is always clearly attributed.
- Where I have quoted from the work of others, the source is always given. With the exception of such quotations, this thesis is entirely my own work.
- I have acknowledged all main sources of help.
- Where the thesis is based on work done by myself jointly with others, I have made clear exactly what was done by others and what I have contributed myself.

Signed: ____

Date: ____

"Write a funny quote here."

If the quote is taken from someone, their name goes here

UNIVERSITY OF FRIBOURG (SWITZERLAND))

Abstract

Faculty Name
Department of Geosciences

Doctor of Philosophy

by Suryanarayanan Balasubramanian

The Thesis Abstract is written here (and usually kept to just this page). The page is kept centered vertically so can expand into the blank space above the title too...

Contents

For/Dedicated to/To my…

Chapter 1

Ice Reservoirs

1.1 Definition

1.2 State of knowledge

1.3 Thesis objectives and structure

For centuries, in the Himalayan mountain ranges, local cultures have believed that glaciers are alive. And what's more, that certain glaciers can have different genders including male and female. These people 'breed' new glaciers by grafting together—or marrying—fragments of ice from male and female glaciers, then covering them with charcoal, wheat husks, cloths, or willow branches so they can reproduce in privacy. These glacierets transform into fully active glaciers that grow each year with additional snowfall. Those then serve as lasting reserves of water that farmers can use to irrigate their crops. Over the years, these practices have inspired other cultures, where people are creating their own artificial ice reservoirs (AIRs) and applying them to solve serious modern challenges around water supplies.

Take Ladakh, a high-altitude desert region in northern India. It sits in the rain shadow of the Himalayas and receives on average fewer than ten centimeters of rain/snow per year. As local glaciers shrink because of climate change, regional water scarcity is increasing. And so, local farmers have started growing their own ice reservoirs as insurance against this uncertainty.

Due to low temperatures and high variability of seasonal snow cover [1], there is a shortage of water at the onset of the agricultural season for about two months until a sufficient and reliable supply of meltwater from high altitude glaciers becomes available.

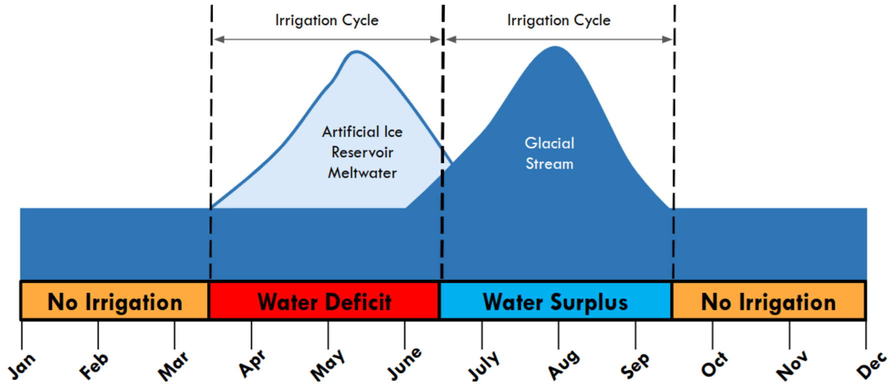

FIGURE 1.1: Seasonal variation in the availability of irrigation water. The graph highlights the crucial role of AIRs in bridging the phase of water scarcity in spring. Adapted from: [2]

AIR serve to bridge this gap in water availability by providing meltwater earlier in the agricultural season. AIRs do so by exploiting gravity and freezing winter temperatures to amass a seasonal stock of ice. Many types of AIRs exist. In the past these were built as horizontal ice sheets much higher up the mountains, making them difficult to manage. Now, as ice cones, they are built next to where the water is needed most, right on the outskirts of villages, near their fields.

While much has been written about the promise of AIRs for irrigation water supply, very little data exists to support these claims. Published quantifications of their water storage capacity differs between 17,000 and 23500 m^3 [3, 4]. Recent research has called for an examination of their long-term efficacy and their usefulness as climate change adaptation strategies [5].

We attempt to address this gap through a measurement campaign of AIRs built in India and Switzerland. This campaign used drones, flowmeters and weather stations to create a calibration and validation dataset for a mass and energy balance model. The parameters of the model were calibrated and its ice volume evolution were validated using this dataset to produced the AIR model.

The influence of meteorological conditions on AIR water-use efficiency and maximum volume was quantified by comparing the modelled volume evolution of Indian AIRs and Swiss AIRs.

The influence of the fountain characteristics on AIR water-use efficiency and maximum volume was quantified by comparing the modelled volume evolution of AIRs produced with different fountain designs and scheduling strategies.

Chapter 2

Religion of ice reservoirs

For centuries, in the Himalayan mountain ranges, local cultures have believed that glaciers are alive. And what's more, that certain glaciers can have different genders including male and female. These people 'breed' new glaciers by grafting together—or marrying—fragments of ice from male and female glaciers, then covering them with charcoal, wheat husks, cloths, or willow branches so they can reproduce in privacy. These glacierets transform into fully active glaciers that grow each year with additional snowfall. Those then serve as lasting reserves of water that farmers can use to irrigate their crops. Over the years, these practices have inspired other cultures, where people are creating their own artificial ice reservoirs (AIRs) and applying them to solve serious modern challenges around water supplies.

2.1 An old history

According to legend, when the people of Baltistan learnt of the Mongol army advancing towards them from the north in the early 13th century, they came up with an ingenious way to stop them. As the inhabited valleys were only accessible through narrow passes, they decided to block the entry way by building a glacier. This successfully prevented the Mongol invasion and, crucially, it also solved the locals' other big problem: water scarcity.

2.2 The marriages of glaciers

The people of Gilgit Baltistan believe that glaciers are living entities. That's why a combination of female and male ice was absolutely necessary. The male glacier – called 'po gang' locally – gives off little water and moves slowly, while a 'female glacier' – or 'mo gang' – is a growing glacier that gives off a lot of water.

The glaciers that people help to grow are the fruit of the sacred union between a mother glacier and a father glacier. They get married and have offspring. The selection of an appropriate site for this marriage is of utmost importance, and a suitable spot must fulfil a list of conditions. It should be located at an altitude of at least 4000 or 5000 metres above sea level; it should be on a gentle slope, where it should have minimal exposure to sunlight, thus a north-facing mountain side is preferable. For most of the expert glacier grafters, the presence of permafrost or ice on the site is another key requirement.

Once a suitable spot is selected, the expedition can be planned. The bride and the groom – the female and the male glacier, preferably from different villages – are chosen and the marriage can be planned. The glacier grafting usually takes place in November, when the local temperatures oscillate around zero. A 12-man party carries the pieces of female ice in woven baskets, another 12 men carry the male ice, the water drawn from the Indus river is carried traditionally in 12 gourd bottles, but sometimes clay pots or goatskins are also required, as well as charcoal and wheat husks or sawdust, which act as insulators for the ice. The last ingredient is salt, which, according to some glacier grafters, helps protect the new glacier from impurities. The bride and groom party walk from different sites and meet in a certain spot to climb together to the glacier growing site, but no greetings are exchanged, as the people involved in the ceremony must remain silent until the ice is deposited in its new home. They walk continuously without having a break, but if the distance is too much and rest is required, they do not put their loads on the ground, instead hanging the baskets on trees, or on walking sticks if nothing else is available. Each man has to carry around 15 to 25 kilograms of ice, walking in cold air, silently up the mountains, for a day or more. Once they reach the glacier growing site, they deposit their valuable loads. The ice lumps and water bottles are placed in between the boulders, or in a small cave, or sometimes in a specially dug pit, and covered with layers of salt, charcoal and sawdust. The silence is broken as religious leaders recite verses of the Quran and say prayers for the success of the glacier marriage and for protection from the djinns. Once the male and female glaciers are placed in their new home and covered, a man from the party of glacier grafters stands up and offers his life for the success of the process. His symbolic sacrifice is matched by the actual sacrifice of a goat – its meat is distributed to a charity, because prayers are more likely to be answered if accompanied by an act of charity. They will not visit the place for at least three years, so as not to disturb the glacier. It is said that a person who disturbs the glacier before its maturation will die. The celebrations continue in the village with traditional songs and prayers, alongside festive food and the joy of the accomplished mission.

2.3 From folklore to science

Myths, legends and superstitions are ways of knowing. But they need to be translated to the language of science. However, when it comes to past projects, there is only anecdotal evidence available.

According to Ingvar Tveiten, a researcher from Norway, the account of the glacier development process presented by a glacier grafter from Balghar bears a strong resemblance to the definition of the formation of rock glaciers. According to a description by a Balghar local: "First the ice slips down into the rocks where it grows roots. Then it starts to break the rocks bringing them up. Then the glacier comes forward. This has happened where they did the glacier growing." Tveiten, who conducted field research in Baltistan, concludes that "glacier growing is typically performed [...] in a terrain that is conducive to the accumulation of snow by avalanching and snow slips. The presence of permafrost at these locations is likely to contribute to ice accumulating [...] Thus, glacier growing is conducted at locations which are already very prone to ice accumulation, and may explain why glacier growing is perceived to work." Here it is, traditional knowledge translated into the language of science.

Even the choice of the glacier grafting site suggests that the technique was developed as a result of the local people's deep understanding of local environmental processes. The view of glaciers as animate implies that humans can influence on the lives of glaciers, just as glaciers can influence on the lives of people.

Chapter 3

Science of ice reservoirs

This chapter provides the methodology used to estimate the ice volume evolution and water-use efficiency of AIRs. The equations governing the mass and energy balance of vertical AIRs (or Icestupas) is explained along with the associated datasets required for forcing, calibration and validation of this AIR model.

The influence of the chosen location and fountain used was quantified by feeding weather and fountain data to an energy balance model and validating the ice volume estimates produced with volume observations from drone flights. Therefore, weather observations and fountain characteristics were required to force the AIR model and ice volume observations were required to calibrate and validate the model.

3.1 Study sites and data

3.1.1 Study sites

We chose two villages in the Swiss Alps and the Indian Himalayas called Guttannen and Gangles to collect the required datasets described above. These two locations exhibit drastically different weather patterns (see Table) owing to their latitude, longitude and altitude differences. This enabled us to highlight the meteorological influences on ice volume evolution (RQ 1).

The Guttannen site (46.66 $N, 8.29$E) is situated in the Berne region, Switzerland and has an altitude of 1047 m a.s.l. In the winter (Oct-Apr), mean daily minimum and maximum air temperatures vary between -13 and 15 . Clear skies are rare, averaging around 7 days during winter. Daily winter precipitation can sometimes be as high as 100 mm. These values are based on 30 years of hourly historical weather data measurements [6].

Several AIRs were constructed by the Guttannen Bewegt Association, the University of Fribourg and the Lucerne University of Applied Sciences and Arts during the winters of 2020-22.

The Gangles site (34.22 N, 77.61E) is located around 20 km north of Leh city in the Ladakh region, lying at 4025 m a.s.l.. The mean annual temperature is 5.6 , and the thermal range is characterized by high seasonal variation. During January, the coldest month, the mean temperature drops to -7.2 . During August, the warmest month, the mean temperature rises to 17.5 [7]. Because of the rain shadow effect of the Himalayan Range, the mean annual precipitation in Leh totals less than 100 mm, and there is high interannual variability. Whereas the average summer rainfall between July and September reaches 37.5 mm, the average winter precipitation between January and March amounts to 27.3 mm and falls almost entirely as snow. AIRs were constructed here as part of the Ice Stupa Competition by the Himalayan Institute of Alternatives, Ladakh (HIAL).

3.1.2 Meteorological data

Air temperature, relative humidity, wind speed, pressure, longwave and global shortwave radiation are required to calculate the surface energy balance of an AIR. The study period starts when the fountain was forst switched on and ends when the respective AIR melted completely. These two dates are denoted as start and expiry dates henceforth. Each AIR is abbreviated based on the country code of the study site with the year of its expiry date.

3.1.3 Fountain observations

The fountain consists of a pipeline and a nozzle. The pipeline has three attributes, namely : discharge rate (Q), height (h) and water temperature (T_F). Discharge rate represents the discharge rate of the water in the fountain pipeline. Height denotes the height of the fountain pipeline installed. Fountain water temperature is the temperature of water droplets produced by the fountain.

The fountain nozzle has three characteristics, namely : the aperture diameter (dia), the spray radius (r) and pressure loss (P) . Spray radius denotes the observed ice radius formed from the fountain water droplets. Pressure loss denotes the loss of water head caused due to the fountain nozzle.

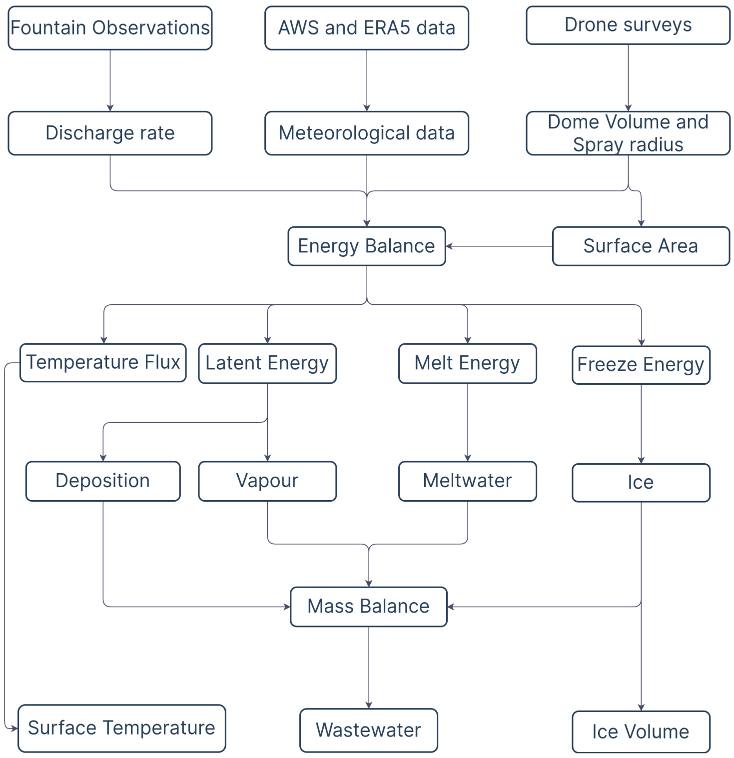

FIGURE 3.1: Model schematic showing the workflow used in the model at every time step.

3.1.4 Drone flights

3.2 AIR Model

A bulk energy and mass balance model is used to calculate the amounts of ice, meltwater, water vapour and wastewater of the AIR. In each hourly time step, the model uses the AIR surface area, energy balance and mass balance calculations to estimate its ice volume, surface temperature and wastewater as shown in Fig. 3.1 .

3.2.1 Surface area calculation

The model assumes the AIR shape to be a cone and assigns the following shape attributes:

$$A^i_{cone} = \pi \cdot r^i_{cone} \cdot \sqrt{(r^i_{cone})^2 + (h^i_{cone})^2} \tag{3.1a}$$

$$V^i_{cone} = \pi/3 \cdot (r^i_{cone})^2 \cdot h^i_{cone} \tag{3.1b}$$

$$j^i_{cone} = \frac{\Delta M^i_{ice}}{\rho_{water} * A^i_{cone}} \tag{3.1c}$$

where i denotes the model time step, r^i_{cone} is the radius; h^i_{cone} is the height; A^i_{cone} is the surface area; V^i_{cone} is the volume and j^i_{cone} is the AIR surface normal thickness change as shown in Fig. 3.2. M^i_{ice} is the mass of the AIR and $\Delta M^i_{ice} = M^{i-1}_{ice} - M^{i-2}_{ice}$. Henceforth, the equations used display the model time step superscript i only if it is different from the current time step.

AIR density can be defined as:

$$\rho_{cone} = \frac{M_F + M_{dep} + M_{ppt}}{(M_F + M_{dep})/\rho_{ice} + M_{ppt}/\rho_{snow}} \tag{3.2}$$

where M_F is the cumulative mass of the fountain discharge; M_{ppt} is the cumulative precipitation; M_{dep} is the cumulative accumulation through water vapour deposition; ρ_{ice} is the ice density (917 $kg\,m^{-3}$) and ρ_{snow} is the density of wet snow (300 $kg\,m^{-3}$) taken from [8] .

AIR volume can also be expressed as:

$$V_{cone} = \frac{M_{ice}}{\rho_{cone}} \tag{3.3}$$

The initial radius of the AIR is assumed to be r_F. The initial height h_0 depends on the dome volume V_{dome} used to construct the AIR as follows:

$$h_0 = \Delta x + \frac{3 \cdot V_{dome}}{\pi \cdot (r_F)^2} \tag{3.4}$$

where Δx is the surface layer thickness (defined in Section 3.2.2)

During the subsequent time steps, the dimensions of the AIR evolve assuming a uniform thickness change (j_{cone}) across its surface area with an invariant slope $s_{cone} = \frac{h_{cone}}{r_{cone}}$. During these time steps, the volume is parameterised using Eqn. 3.1b as:

$$V_{cone} = \frac{\pi \cdot (r_{cone})^3 \cdot s_{cone}}{3} \tag{3.5}$$

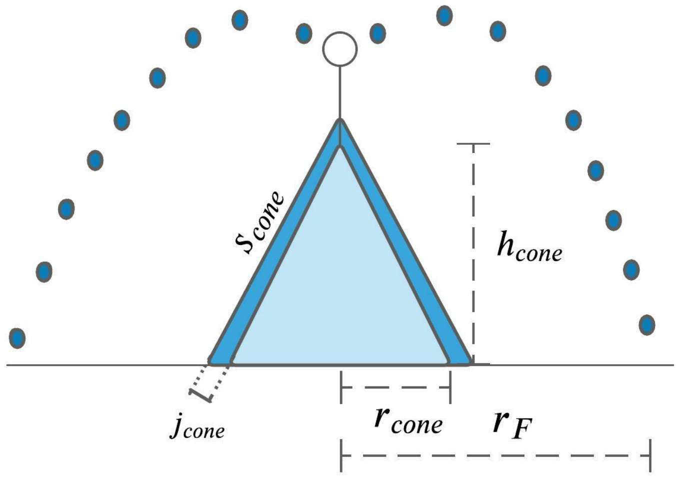

FIGURE 3.2: Shape variables of the AIR. r_{cone} is the radius, h_{cone} is the height, j_{cone} is the thickness change and s_{cone} is the slope of the ice cone. r_F is the spray radius of the fountain.

We define the Icestupa boundary through its spray radius, i.e. we assume ice formation is negligible when $r_{cone} > r_F$. Combining Eqns. 3.1b, 3.3, 3.4 and 3.5, the geometric evolution of the Icestupa at each time step i can be determined by considering the following rules:

$$(r_{cone},\, h_{cone}) = \begin{cases} (r_F,\, h_0) & \textit{if } i = 0 \\ (r_{cone}^{i-1},\, \frac{3 \cdot M_{ice}}{\pi \cdot \rho_{ice} \cdot (r_{cone}^{i-1})^2}) & \textit{if } r_{cone}^{i-1} \geq r_F \textit{ and } \Delta M_{ice} > 0 \\ (\frac{3 \cdot M_{ice}}{\pi \cdot \rho_{ice} \cdot s_{cone}})^{1/3} \cdot (1,\, s_{cone}) & \textit{otherwise} \end{cases} \tag{3.6}$$

3.2.2 Energy balance calculation

We approximate the energy balance at the surface of an AIR by a one-dimensional description of energy fluxes into and out of a (thin) layer with thickness Δx:

$$\rho_{ice} \cdot c_{ice} \cdot \frac{\Delta T}{\Delta t} \cdot \Delta x = q_{SW} + q_{LW} + q_L + q_S + q_F + q_R + q_G \tag{3.7}$$

Upward and downward fluxes relative to the ice surface are positive and negative, respectively. The first term is the energy change of the surface layer, which can be translated into a phase change energy should phase changes occur; q_{SW} is the net shortwave radiation; q_{LW} is the net longwave radiation; q_L and q_S are the turbulent latent and sensible heat fluxes. q_F and q_R represent the heat exchange of the fountain water droplets and rain droplets with the AIR ice surface respectively. q_G represents ground heat flux between the AIR surface and its interior.

The energy flux acts upon the AIR surface layer, which has an upper and lower boundary defined by the atmosphere and the ice body of the AIR, respectively. A sensitivity analysis was later performed to understand the influence of this factor and decide its value. Here, we define the surface temperature T_{ice} to be the modelled average temperature of the icestupa surface layer.

3.2.2.1 Net Shortwave Radiation q_{SW}

The net shortwave radiation q_{SW} is computed as follows:

$$q_{SW} = (1 - \alpha) \cdot (SW_{direct} \cdot f_{cone} + SW_{diffuse}) \tag{3.8}$$

where SW_{direct} and $SW_{diffuse}$ are the direct and diffuse shortwave radiation, α is the modelled albedo and f_{cone} is the area fraction of the ice structure exposed to the direct shortwave radiation.

The albedo varies depending on the water source that formed the current AIR surface layer. During the fountain runtime, the albedo assumes a constant value corresponding to ice albedo. However, after the fountain is switched off, the albedo can reset to snow albedo during snowfall events and then decay back to ice albedo. We use the scheme described in [9] to model this process. The scheme records the decay of albedo with time after fresh snow is deposited on the surface. δt records the number of time steps after the last snowfall event. After snowfall, albedo changes over a time step, δt , as

$$\alpha = \alpha_{ice} + (\alpha_{snow} - \alpha_{ice}) \cdot e^{(-\delta t)/\tau} \tag{3.9}$$

where α_{ice} is the bare ice albedo value (0.25), α_{snow} is the fresh snow albedo value (0.85) and τ is a decay rate (16 *days*), which determines how fast the albedo of the ageing snow recedes back to ice albedo. Discharge events decrease the decay rate by a factor of $\alpha_{ice}/\alpha_{snow}$.

The solar area fraction f_{cone} of the ice structure exposed to the direct shortwave radiation depends on the shape considered. Using the solar elevation angle θ_{sun}, the solar beam can be considered to have a vertical component, impinging on the horizontal surface (semicircular base of the AIR), and a horizontal component impinging on the vertical cross section (a triangle). The solar elevation angle θ_{sun} used is modelled using the parametrisation proposed by [10]. Accordingly, f_{cone} is determined as follows:

$$f_{cone} = \frac{(0.5 \cdot r_{cone} \cdot h_{cone}) \cdot cos\theta_{sun} + (\pi \cdot (r_{cone})^2/2) \cdot sin\theta_{sun}}{\pi \cdot r_{cone} \cdot ((r_{cone})^2 + (h_{cone})^2)^{1/2}} \tag{3.10}$$

The diffuse shortwave radiation is assumed to impact the conical AIR surface uniformly.

3.2.2.2 Net Longwave Radiation q_{LW}

The net longwave radiation q_{LW} is determined as follows:

$$q_{LW} = LW_{in} - \sigma \cdot \epsilon_{ice} \cdot (T_{ice} + 273.15)^4 \tag{3.11}$$

where T_{ice} is the modelled surface temperature given in [], $\sigma = 5.67 \cdot 10^{-8}\, Jm^{-2}s^{-1}K^{-4}$ is the Stefan-Boltzmann constant, LW_{in} denotes the incoming longwave radiation and ϵ_{ice} is the corresponding emissivity value for the Icestupa surface (0.97).

The incoming longwave radiation LW_{in} for the Indian site, where no direct measurements were available, is determined as follows:

$$LW_{in} = \sigma \cdot \epsilon_a \cdot (T_a + 273.15)^4 \tag{3.12}$$

here T_a represents the measured air temperature and ϵ_a denotes the atmospheric emissivity. We approximate the atmospheric emissivity ϵ_a using the equation suggested by [11], considering air temperature and vapor pressure (Eqn. 3.13). The vapor pressure of air over water and ice was obtained using Eqn. 3.16. The expression defined in [12] for clear skies (first term in equation 3.13) is extended with the correction for cloudy skies after [11] as follows:

$$\epsilon_a = 1.24 \cdot (\frac{p_{v,w}}{(T_a + 273.15)})^{1/7} \cdot (1 + 0.22 \cdot cld^2) \tag{3.13}$$

with a cloudiness index cld, ranging from 0 for clear skies to 1 for complete overcast skies. For the Indian site, we assume cloudiness to be negligible.

3.2.2.3 Turbulent fluxes

The turbulent sensible q_S and latent heat q_L fluxes are computed with the following expressions proposed by [13]:

$$q_S = \mu_{cone} \cdot c_a \cdot \rho_a \cdot p_a/p_{0,a} \cdot \frac{\kappa^2 \cdot v_a \cdot (T_a - T_{ice})}{(\ln \frac{h_{AWS}}{z_0})^2} \tag{3.14}$$

$$q_L = \mu_{cone} \cdot 0.623 \cdot L_s \cdot \rho_a/p_{0,a} \cdot \frac{\kappa^2 \cdot v_a(p_{v,w} - p_{v,ice})}{(\ln \frac{h_{AWS}}{z_0})^2} \tag{3.15}$$

where h_{AWS} is the measurement height above the ground surface of the AWS (around $2\,m$ for all sites), v_a is the wind speed in $[m\,s^{-1}]$, c_a is the specific heat of air at constant pressure (1010 J $kg^{-1}K^{-1}$), ρ_a is the air density at standard sea level (1.29 kgm^{-3}), $p_{0,a}$ is the air pressure at standard sea level (1013 hPa), p_a is the measured air pressure, κ is the von Karman constant (0.4), z_0 is the surface roughness (3 mm) and L_s is the heat of sublimation (2848 $kJ\,kg^{-1}$). The vapor pressure of air with respect to water ($p_{v,w}$) and with respect to ice ($p_{v,ice}$) was obtained using the formulation given in [14] :

$$\begin{aligned} p_{v,w} &= e^{\frac{(34.494 - \frac{4924.99}{T_a + 237.1})}{(T_a+105)^{1.57} \cdot 100}} \cdot \frac{RH}{100} \\ p_{v,ice} &= e^{\frac{(43.494 - \frac{6545.89}{T_{ice}+278})}{(T_{ice}+868)^2 \cdot 100}} \end{aligned} \tag{3.16}$$

The dimensionless parameter μ_{cone} is an exposure parameter that deals with the fact that AIR has a rough appearance and forms an obstacle to the wind regime. This factor accounts for the larger turbulent fluxes due to the roughness of the surface [15], and is a function of the AIR slope as follows:

$$\mu_{cone} = 1 + \frac{s_{cone}}{2} \tag{3.17}$$

A possible source of error is the fact that wind measurements from the horizontal plane at the AWS are used, which might be different from those on a slope. However, without detailed datasets from the AIR surface, we retain this assumption.

3.2.2.4 Fountain discharge heat flux q_F

The fountain water, at temperature T_F, is assumed to cool to 0 . Thus, the heat flux caused by this process is:

$$q_F = \frac{\Delta M_F \cdot c_{water} \cdot T_F}{\Delta t \cdot A_{cone}} \tag{3.18}$$

with c_{water} as the specific heat of water (4186 J $kg^{-1}K^{-1}$).

3.2.2.5 Rain heat flux q_R

The influence of rain events on the albedo and the energy balance was assumed to be similar to that of discharge events. However, the water temperature of a ran event was assumed to equal to the air temeperature. Accordingly, the heat flux generated due to a rain event was equal to:

$$q_R = \frac{\Delta M_{ppt} \cdot c_{water} \cdot T_a}{\Delta t \cdot A_{cone}} \tag{3.19}$$

3.2.2.6 Bulk Icestupa heat flux q_G

The bulk Icestupa heat flux q_G corresponds to the ground heat flux in normal soils and is caused by the temperature gradient between the surface layer (T_{ice}) and the ice body (T_{bulk}). It is expressed by using the heat conduction equation as follows:

$$q_G = k_{ice} \cdot (T_{bulk} - T_{ice}^{i-1})/l_{cone} \tag{3.20}$$

where k_{ice} is the thermal conductivity of ice (2.123 $W\,m^{-1}\,K^{-1}$) , T_{bulk} is the mean temperature of the ice body within the icestupa and l_{cone} is the average distance of any point in the surface to any other point in the ice body. T_{bulk} is initialised as 0 and later determined from Eqn. 3.20 as follows:

$$T_{bulk}^{i+1} = T_{bulk} - (q_G \cdot A \cdot \Delta t)/(M_{ice} \cdot c_{ice}) \tag{3.21}$$

Since AIRs typically have conical shapes with $r_{cone} > h_{cone}$, we assume that the center of mass of the cone body is near the base of the fountain. Thus, the distance of every point in the AIR surface layer from the cone body's center of mass is between h_{cone} and r_{cone}. Therefore, we calculate q_G assuming $l_{cone} = (r_{cone} + h_{cone})/2$.

3.2.2.7 Phase changes

In this section, the numerical procedures to model phase changes at the surface layer are explained. Let T_{temp} be the calculated surface temperature. Therefore, Eqn. 3.7 can be rewritten as:

$$q_{total} = \rho_{ice} \cdot c_{ice} \cdot \frac{(T_{temp} - T_{ice})}{\Delta t} \cdot \Delta x$$

where q_{total} represents the total energy available to be redistributed. Even if the numerical heat transfer solution produces temperatures which are $T_{temp} > 0$, say from intense shortwave radiation, the ice temperature must remain at $T_{temp} = 0$. The "excess" energy is used to drive the melting process. Moreover, the energy input is used to melt the surface ice layer, and not to raise the surface temperature to some unphysical value. Similarly, for freezing to occur, three conditions are required. Firstly, fountain water is present $(\Delta M_F > 0)$ and secondly the calculated temperature of the ice, T_{temp}, is below 0. However, these two conditions are not sufficient as the latent heat turbulent fluxes can only contribute to temperature fluctuations. Therefore, an additional condition, namely, $(q_{total} - q_L) < 0$, is required. Depending on the above conditions, the total energy q_{total} can be redistributed for the melting (q_{melt}), freezing (q_{freeze}) and surface temperature change (q_T) processes as follows:

$$q_{total} = \begin{cases} q_{freeze} + q_T & \textit{if } \Delta M_F > 0 \textit{ and } T_{temp} < 0 \textit{ and } (q_{total} - q_L) < 0 \\ q_{melt} + q_T & \textit{otherwise} \end{cases} \tag{3.22}$$

Henceforth, time steps when the the total energy is redistributed to the freezing energy are called freezing events and the rest of the time steps are called melting events.

During a freezing event, the AIR surface is assumed to warm to 0. The available energy $(q_{total} - q_L)$ is further increased due to this change in surface temperature represented by the energy flux:

$$q_0 = \frac{\rho_{ice} \cdot \Delta x \cdot c_{ice} \cdot T_{ice}^{i-1}}{\Delta t}$$

The available fountain discharge (ΔM_F) may not be sufficient to utilize all the freezing energy. At such times, the additional freezing energy further cools down the surface temperature. Accordingly, the surface energy flux distribution during a freezing event can be represented as:

$$(q_{freeze}, q_T) = \begin{cases} (\frac{\Delta M_F \cdot L_f}{A_{cone} \cdot \Delta t}, q_{total} + \frac{\Delta M_F \cdot L_f}{A_{cone} \cdot \Delta t}) & if\ \Delta M_F\ insufficient \\ (q_{total} - q_L + q_0, q_L - q_0) & otherwise \end{cases} \tag{3.23}$$

If $T_{temp} > 0$, then energy is reallocated from q_T to q_{melt} to maintain surface temperature at melting point. The total energy flux distribution during a melting event can be represented as:

$$(q_{melt}, q_T) = \begin{cases} (0, q_{total}) & if\ T_{temp} \leq 0 \\ (\frac{T_{temp} \cdot \rho_{ice} \cdot c_{ice} \cdot \Delta x}{\Delta t}, q_{total} - \frac{T_{temp} \cdot \rho_{ice} \cdot c_{ice} \cdot \Delta x}{\Delta t}) & if\ T_{temp} > 0 \end{cases} \tag{3.24}$$

3.2.3 Mass balance calculation

The mass balance equation for an AIR is represented as:

$$\frac{\Delta M_F + \Delta M_{ppt} + \Delta M_{dep}}{\Delta t} = \frac{\Delta M_{ice} + \Delta M_{water} + \Delta M_{sub} + \Delta M_{waste}}{\Delta t} \tag{3.25}$$

where M_F is the cumulative mass of the fountain discharge; M_{ppt} is the cumulative precipitation; M_{dep} is the cumulative accumulation through water vapour deposition; M_{ice} is the cumulative mass of ice; M_{water} is the cumulative mass of melt water; M_{sub} represents the cumulative water vapor loss by sublimation and M_{waste} represents the fountain wastewater that did not interact with the AIR. The left hand side of equation 3.25 represents the rate of mass input and the right hand side represents the rate of mass output for an AIR.

Precipitation input is calculated as shown in equation 3.26b where ρ_w is the density of water (1000 $kg\, m^{-3}$), $\Delta ppt/\Delta t$ is the measured precipitation rate in $[m\, s^{-1}]$ and T_{ppt} is the temperature threshold below which precipitation falls as snow. Here, snowfall events were identified using T_{ppt} as 1. Snow mass input is calculated by assuming a uniform deposition over the entire circular footprint of the AIR.

The latent heat flux is used to estimate either the evaporation and condensation processes or sublimation and deposition processes as shown in equation 3.26c. During the time steps at which the surface temperature is below 0 only sublimation and deposition can occur, but if the surface temperature reaches 0 , evaporation and condensation can also occur. As the differentiation between evaporation and sublimation (and condensation and deposition) when the air temperature reaches 0 is challenging, we assume that negative (positive) latent heat fluxes correspond only to sublimation (deposition), i.e. no evaporation (condensation) is calculated.

Since we have categorized every time step as a freezing or melting event, we can determine the melting/freezing rates and the corresponding meltwater/ice quantities as shown in equations 3.26e, 3.26d and 3.26f. Having calculated all other mass components, the fountain wastewater generated every time step can be calculated using Eqn. 3.25.

$$\frac{\Delta M_F}{\Delta t} = \begin{cases} \frac{60}{\rho_w \cdot \Delta t} \cdot d_F & \textit{if fountain is on} \\ 0 & \textit{otherwise} \end{cases} \tag{3.26a}$$

$$\frac{\Delta M_{ppt}}{\Delta t} = \begin{cases} \pi \cdot (r_{cone})^2 \cdot \rho_w \cdot \frac{\Delta ppt}{\Delta t} & \textit{if } T_a < T_{ppt} \\ 0 & \textit{if } T_a \geq T_{ppt} \end{cases} \tag{3.26b}$$

$$(\frac{\Delta M_{dep}}{\Delta t}, \frac{\Delta M_{sub}}{\Delta t}) = \begin{cases} \frac{q_L \cdot A_{cone}}{L_s} \cdot (1, 0) & \textit{if } q_L \geq 0 \\ \frac{q_L \cdot A_{cone}}{L_s} \cdot (0, -1) & \textit{if } q_L < 0 \end{cases} \tag{3.26c}$$

$$\frac{\Delta M_{water}}{\Delta t} = \frac{q_{melt} \cdot A_{cone}}{L_f} \tag{3.26d}$$

$$\frac{\Delta M_{freeze/melt}}{\Delta t} = \frac{q_{freeze/melt} \cdot A_{cone}}{L_f} \tag{3.26e}$$

$$\frac{\Delta M_{ice}}{\Delta t} = \frac{q_{freeze} \cdot A_{cone}}{L_f} + \frac{\Delta M_{ppt}}{\Delta t} + \frac{\Delta M_{dep}}{\Delta t} - \frac{\Delta M_{sub}}{\Delta t} - \frac{\Delta M_{water}}{\Delta t} \tag{3.26f}$$

Considering AIRs as water reservoirs, their net water loss can be defined as:

$$\textit{Net water losses} = \frac{M_{waste} + M_{sub}}{(M_F + M_{ppt} + M_{dep})} \cdot 100 \tag{3.27}$$

3.3 Cosistupa model

3.4 Suggestions for future measurement campaigns

3.4.1 Further Data acquisition

3.4.1.1 Measurement of meltwater quantities

3.4.1.2 Measurement of fountain characteristics

3.4.1.3 Drone flight analysis

3.4.2 Improvement of model algorithm

3.4.2.1 Initialisation of model

3.4.2.2 Better model parametrisations

Chapter 4

Habitat of ice reservoirs

AIRs cannot be built anywhere. They require a water source sufficiently above and weather conditions cold enough to amass a seasonal stock of ice. This imposes several meteorological and topographical requirements for the chosen construction location. The meteorological requirements can be used to identify favourable regions worldwide whereas the topographical requirements can be used to pinpoint the construction site within the respective region. Below we detail these requirements and propose methodologies for finding construction sites satisfying them.

4.1 Requirements for AIR construction

4.1.1 Meteorological requirements

AIRs prefer colder, drier and less-cloudy regions. Our results quantify this preference based on maximum ice volume estimations of the Swiss and the Indian AIRs (see Paper I). The Swiss AIRs have little utility as a water reservoir due to their small size and short survival duration. Therefore, construction of AIRs should not be carried out in locations less favourable than the Swiss site.

4.1.2 Topographical requirements

The water source of an AIR could be either a spring, stream or lake. Springs are the ideal water source since they are easy to transport via pipelines to the construction site due to their relatively warm temperatures. Other water sources tend to freeze within the pipeline during tranport. It is pointless to use lakes as water sources unless there is utility in draining and converting them to ice structures. This is the case for glacial lakes which can be drained to prevent flash floods while using the water supply to harvest ice structures.

AIRs prefer shadowed valleys. This is because their melt rate is driven by solar radiation (see Paper I).

4.2 Quantifying AIR construction potential of any locations

However, it is challenging to determine a methodology to compare meteorological conditions of two locations. Our suggested methodology is described in

Chapter 5

Technology of ice reservoirs

AIRs are a natural evolution of Ladakh's agricultural system. They can be related to traditional water harvesting technologies like the zing, which are small tanks where meltwater is collected through the use of an expensive and intricate network of channels. The mountain oases of the Hindu Kush and Karakoram ranges have similar irrigation networks [2].

5.1 Ice terraces

5.1.1 Invention

Ice terraces are the oldest form of AIRs [16]. They used these irrigation networks to amass a seasonal stock of ice by exploiting gravity and freezing winter temperatures. Chewang Norphel, a well known engineer of the Leh Nutrition Project, introduced this innovation of local technology to Ladakh in the 1980s and 1990s [17].

5.1.2 Construction strategy

These structures were built on south-facing slopes as a cascading series of rock walls in the river beds to reduce runoff velocity and guide meltwater into shadowed areas (see Fig. 5.1). The resulting shallow pools begin to freeze as temperatures drop in winter, and ice accumulates.

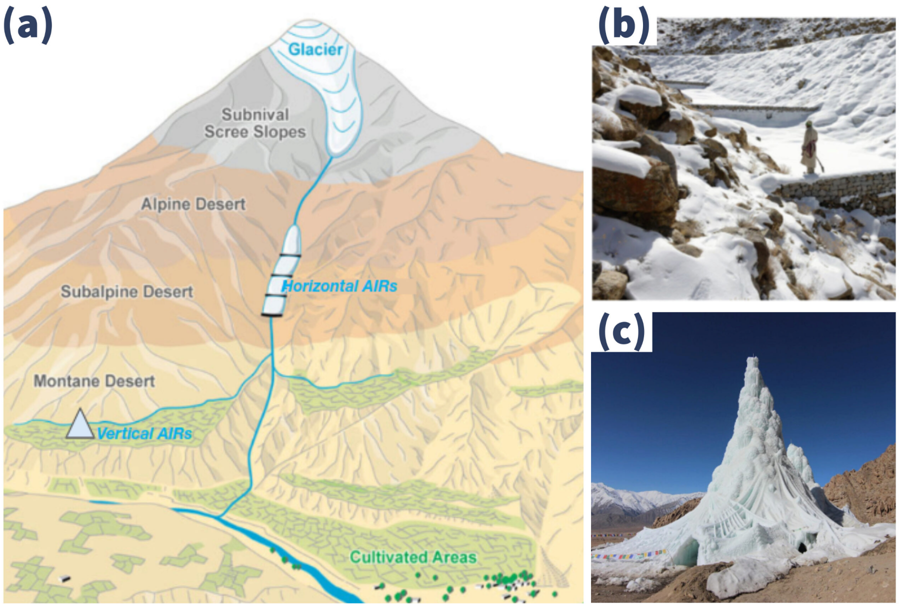

FIGURE 5.1: (a) Schematic overview of the position of artificial ice reservoirs. These constructions are located at altitudes between the glaciers and the irrigation networks in the cultivated areas. (b) Horizontal ice reservoirs at 3900 m, located above the village of Nang, Ladakh. The cascade is composed of a series of loose masonry walls ranging in height from 2 to 3 m, which help freeze water for storage. (c) Vertical ice reservoirs at 3600 m, located above the village of Phyang, Ladakh. They are made using fountain systems. Adapted from: [2]

5.1.3 Application

5.1.4 Drawbacks

However, the location requirements and the construction cost of ice terraces were prohibitive for widespread adoption.

5.1.5 Suggestions for improvement

5.2 Ice stupas

5.2.1 Invention

This prompted the invention of Ice stupas by Sonam Wangchuk in 2013 **??**. Due to their shape, Ice stupas could be built adjacent to the irrigated plantations. It was also relatively cheaper. A typical Ice stupa just requires a fountain nozzle mounted on a supply pipeline. The water source is usually a spring or a glacial stream. Due to the altitude difference between the pipeline input and fountain output, water ejects from the fountain nozzle as droplets that eventually lose their energy and accumulate as ice. The fountain is manually activated during the winter nights and is raised, through addition of metal pipes, when significant ice accumulates below.

5.2.2 Construction strategy

5.2.3 Application

5.2.4 Drawbacks

5.2.5 Suggestions for improvement

Chapter 6

Heritage of ice reservoirs

This chapter provides conclusions based on research findings from data collected on AIRs in Switzerland and India, as well as discussion and recommendations for future research. This Chapter will review the purpose of the study, research questions, literature review, and findings of the study. It will then present conclusions, discussion of the conclusions, and recommendations for practice and for further research.

6.1 Summary

Cryosphere fed irrigation networks are completely dependant on the timely availability of meltwater from glaciers, snow and permafrost. With the accelerated decline of glaciers, these irrigation networks can no longer deliver adequate water to sustain agricultural output and take advantage of the complete growing season. As a consequence, some mountain villages have either been abandoned or lie on the brink of desertification.

In the past few decades, artificial ice reservoir (AIR) technologies have provided much needed relief to these water-stressed communities. These strategies revolve around augmenting their glacial ice reservoirs with man-made ones that provide supplementary irrigation during the spring. In the context of the observed present and predicted global glacier shrinkage, the development of such water storage technologies is crucial to ensure continued survival of mountain communities.

Because small-scale processes, complex feedbacks and non-linearities govern their evolution, accessing the response of AIRs to the location and fountain chosen is challenging and only feasible if backed up with comprehensive field data. However, empirical data and studies focussing on AIRs are sparse.

A measurement campaign was performed using drones, flowmeters and weather stations on almost a dozen AIRs across two locations (India and Switzerland), over four winters (2019, 2020, 2021 and 2022) and using two different construction methods (traditional and automated). The corresponding datasets were codenamed with the prefix of the country, the suffix of the winter season and the construction method used (eg. Traditional CH21 AIR). AIR radius, area and volume were recorded using DEMs produced from drone flights. The fountain characteristics were calibrated from the observed radius and discharge rates. The model parameters were calibrated from some volume observations. The rest of this DEM dataset were used to validate the modelled volume evolution. This provided a unique data basis for quantifying the feasibility and potential of this water storage technology worldwide.

Physical models provide unbiased insight into the physical processes and the drivers of temporal and spatial changes. With a special focus on icestupas, here defined as vertical AIRs, a mass and energy balance model was developed and used as a tool to quantify the influence of meteorological conditions and fountain characteristics. The model has been shown to perform excellently when calibrated with field data. It could be shown that the maximum volume of AIRs located in the IN and CH regions differ by an order of magnitude. The differences can be attributed to the stronger sublimation process due to the colder and drier weather conditions of the IN region.

AIR maintenance requirement was reduced and their fountain freezing events were prevented by developing an automated construction strategy. This improved construction strategy made fountain operation weather-sensitive through the use of an automation system that scheduled discharge rates based on the recommendations of the AIR model. The automated construction strategy was successful in making AIRs using 87 % less water while being maintenance-free.

A spirit of improvisation guides the design and construction of AIRs making it difficult to make a quantitative comparison from site to site. A holistic approach is required which uses the topographical conditions and water demands of the construction site to choose the appropriate construction methodology and form of ice reservoir to be produced.

6.2 Conclusions

The main objective of this thesis was to improve our understanding about the response of AIRs to changes in their construction location and fountain characteristics. In a first experiment, the evolutional of AIRs in Indian Himalayas and the Swiss Alps are compared. The model results show:

- Icestupa's maximum volume can vary by an order of magnitude due to meteorological conditions of their contruction location.
- Icestupa fountain systems spray five times more water than required.

In a second experiment, the evolution of AIRs using different fountain scheduling strategies are compared. The model results show:

- Weather-sensitive fountain systems increase AIR water-use efficiency 8 fold.
- Weather-sensitive fountain systems enable maintenance-free AIR construction.

6.3 Discussion

6.4 Recommendations

- Colder, drier and less cloudy construction locations form long-lasting AIRs with higher maximum ice volumes.
- Weather-sensitive fountain systems produce larger and efficient AIRs effortlessly.

6.5 Suggestions for future research

- Identification of favourable locations.
- Cosistupa model development.

6.6 Final thoughts

Papers

The acknowledgements and the people to thank go here, don't forget to include your project advisor…

The Cryosphere, 15, 3007–3012, 2021
https://doi.org/10.5194/tc-15-3007-2021

The Cryosphere
Open Access

Brief communication: Growth and decay of an ice stupa in alpine conditions – a simple model driven by energy-flux observations over a glacier surface

Johannes Oerlemans[1], **Suryanarayanan Balasubramanian**[2], **Conradin Clavuot**[3], **and Felix Keller**[4,5]

[1]Institute for Marine and Atmospheric Research, Utrecht University, Princetonplein 5, Utrecht, 3585CC, the Netherlands
[2]Department of Geosciences, University of Fribourg, Fribourg, Switzerland
[3]Architecture Clavuot, Gäugelistrasse 49, Chur 7000, Switzerland
[4]Academia Engiadina, Samedan, Switzerland
[5]Department of Environmental Systems Science, ETH, Zurich, Switzerland

Correspondence: Johannes Oerlemans (j.oerlemans@uu.nl)

Received: 13 February 2021 – Discussion started: 1 April 2021
Revised: 30 May 2021 – Accepted: 4 June 2021 – Published: 29 June 2021

Abstract. We present a simple model to calculate the evolution of an ice stupa (artificial ice reservoir). The model is formulated for a cone geometry and driven by energy balance measurements over a glacier surface for a 5-year period. An "exposure factor" is introduced to deal with the fact that an ice stupa has a very rough surface and is more exposed to wind than a flat glacier surface. The exposure factor enhances the turbulent fluxes.

For characteristic alpine conditions at 2100 m, an ice stupa may reach a volume of 200 to 400 m^3 in early April. We show sensitivities of ice stupa size to temperature changes and exposure factor. The model may also serve as an educational tool, with which the effects of snow cover, switching off water during daytime, different starting dates, switching off water during high wind speeds, etc. can easily be evaluated.

1 Introduction

Ice stupas (Fig. 1), also referred to as artificial ice reservoirs (AIRs), are used more and more as a means to store water in the form of ice (Nüsser et al., 2018). In Ladakh, India, engineer Sonam Wangchuk initiated and developed the use of ice stupas to provide water for irrigation purposes in spring and early summer. The ice stupas grow in winter by sprinkling water on the growing ice structure, and they melt in spring and summer to deliver water; a typical turnover volume is up to 1×10^6 L. Ice stupas also form interesting touristic attractions with a distinct and special artistic flavour. They come in the same class as ice sculptures, which are popular in all regions of the world that have a cold winter.

The possibility to grow ice stupas of appreciable size depends on the meteorological conditions and the availability of water. When a surface has a negative energy balance and water is sprayed on it, ice will form (a well-known technique to make skating rinks). The more effective the latent heat of fusion can be removed by contact with cold air and effective emittance of longwave radiation, the faster the ice layer may grow. In spring and summer incoming solar radiation will dominate and the ice stupa will lose mass.

In this note we present a model of ice stupa growth and decay, based on a simple consideration of the total energy budget, and driven by energy flux observations over a glacier surface (half hourly observations over a 5-year period). We believe that the energy balance of a glacier surface and of an ice stupa have much in common and therefore consider this data set as ideal for a first study. The focus is on alpine conditions at a typical height of 2100 m a.s.l. The purpose of this study is to obtain first-order estimates of how fast an ice stupa may grow and melt and what processes are most important. We emphasize that in this note the focus is on the energetics of the ice stupa system, not on the technical aspects that have to be dealt with in constructing an ice stupa.

Published by Copernicus Publications on behalf of the European Geosciences Union.

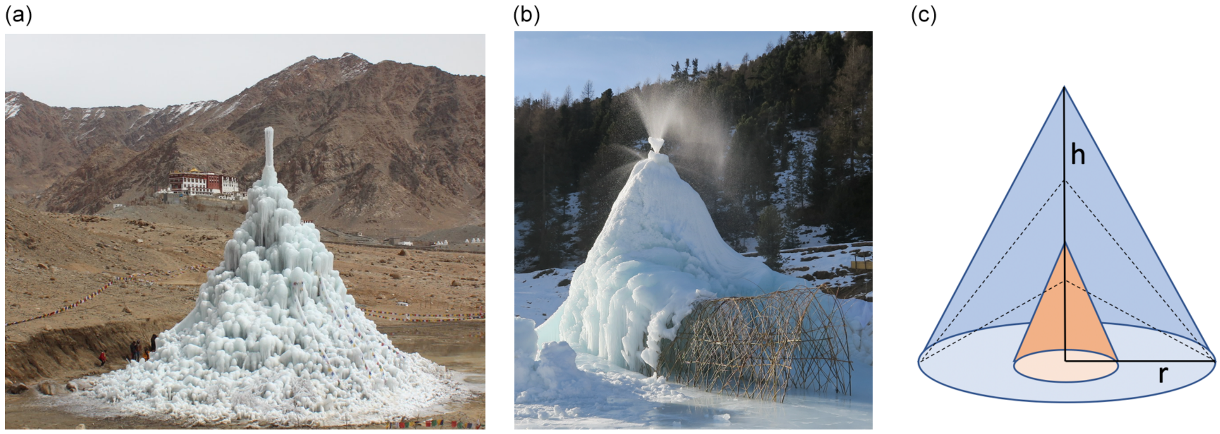

Figure 1. (a) Ice stupa in Ladakh, India (courtesy of Sonam Wangchuk). **(b)** Early growing stage of ice stupa with inner structure in Val Roseg, Switzerland (courtesy of Conradin Clavuot). **(c)** Simple geometrical representation. The ice stupa can have an inner structure (brown). The dashed lines illustrate the growth of an ice stupa from a base with a constant radius.

2 Geometry

Ice stupas have different and often complex shapes. The *cone* is probably the most appropriate simple geometric shape to represent an ice stupa (Fig. 1), but alternatively a *dome* (half sphere) could also be considered.

The geometric characteristics of a cone with radius r and height h are

$$\text{Area of base: } \pi r^2, \quad (1a)$$

$$\text{Lateral area: } \pi r \sqrt{r^2 + h^2}, \quad (1b)$$

$$\text{Volume: } \pi r^2 h/3. \quad (1c)$$

It is useful to introduce a shape parameter $s = h/r$. The volume can then also be written as

$$V = \pi h^3 / 3s^2. \quad (2)$$

So for a given volume the height of the ice stupa can be calculated from

$$h = \left\{ \frac{3}{\pi} V s^2 \right\}^{1/3}. \quad (3)$$

In this note we will consider two cases: (i) the shape factor is constant during growth and decay, and (ii) the ice stupa grows upward from a base with a fixed radius, implying that the shape factor gradually increases. The first case may be more appropriate when an inner structure is used or when water supply is by varying sprinkler properties or even manually. Case (ii) describes better the situation when a fixed spray radius is maintained during the growth phase.

3 Energy exchange

Ice stupas exchange energy with the surroundings by absorbing and reflecting solar radiation, absorbing and emitting longwave (terrestrial) radiation, and by turbulent fluxes of sensible and latent heat. Because of the complex shape of an ice stupa, as compared to a horizontal ice/snow surface, it is hard to describe these processes in detail. However, some simplifying assumptions may help to arrive at reasonable approximations.

We use 5 years of energy balance measurements with an automatic weather station (AWS) on the Vadret da Morteratsch (Morteratsch Glacier) (e.g. Oerlemans et al., 2009), which was located at an elevation of about 2280 m a.s.l. The surface energy flux is written as

$$\text{energy flux} = S_{\text{in}} - S_{\text{out}} + L_{\text{in}} - L_{\text{out}} + H + G. \quad (4)$$

S_{in} stands for solar radiation, S_{out} for reflected solar radiation, L_{in} for incoming longwave radiation, L_{out} for emitted longwave radiation, H for the total turbulent heat flux, and G for the ground heat flux (conduction from or into the surface layer – generally small compared to the other components). These quantities are normally expressed in W m^{-2}. So the energy flux is positive when directed towards the surface. A positive energy flux will be used for melting of ice or snow; when the energy flux is negative freezing of water can take place (when available).

We now discuss how these measurements over (almost) flat terrain can be applied to an ice stupa. We first deal with solar radiation and consider the direct part (fraction q) and diffuse part (fraction $1 - q$) separately. Although the ratio of direct to diffuse solar radiation depends strongly on cloud conditions, outside subtropical climate zones where low cloudiness prevails the components are typically of the same order of magnitude (e.g. Li et al., 2015; Berrizbeitia et al., 2020).

With respect to direct solar radiation, the solar beam can be considered to have a vertical component, impinging on the horizontal surface (base of the ice stupa), and a horizontal component impinging on the vertical cross section (a triangle). Measurements over a flat surface, like those from the glacier AWS, thus underestimate the solar radiation intercepted by an ice stupa. A correction factor f is therefore needed with which the direct radiation as measured by the AWS has to be multiplied. This factor may be large for a low sun, but in alpine conditions where there is always significant shading by the surroundings this situation is rarely found. A simple analysis shows that, for a shape factor of $s = 2$, f varies from 2.5 for a solar elevation of 20° to about 1.2 for a solar elevation of 60°. To account for the fact that the correction factor should be 1 for a flat surface and increase with the shape factor, we use (note that f and s are dimensionless)

$$f = 1 + s/4. \tag{5}$$

For the *diffuse* part of the solar radiation, illumination is on all sides and the relevant area therefore is the lateral area as given in Eq. (1b). Therefore the total amount of absorbed solar radiation per unit of time can be estimated as (in J s^{-1})

$$F_{\mathrm{sol}} = f q\,(S_{\mathrm{in}} - S_{\mathrm{out}})\,\pi r^2 + (1-q)\,(S_{\mathrm{in}} - S_{\mathrm{out}})\,\pi r \sqrt{r^2 + h^2}. \tag{6}$$

Alternatively, one may wish to prescribe the albedo α separately, i.e.

$$F_{\mathrm{sol}} = f q S_{\mathrm{in}}(1-\alpha)\pi r^2 + (1-q) S_{\mathrm{in}}(1-\alpha)\pi r \sqrt{r^2 + h^2}. \tag{7}$$

For the longwave radiation and turbulent exchange, the exposed surface is also the lateral area. The longwave radiation balance then becomes

$$F_{\mathrm{lw}} = (L_{\mathrm{in}} - L_{\mathrm{out}})\pi r \sqrt{r^2 + h^2}. \tag{8}$$

The turbulent heat fluxes depend on the roughness and exposure of the surface. Since we do not calculate the surface (skin) temperature, we simply assume that it is close to the melting point. The sensible and latent heat input are calculated using the well-known bulk transfer equations (e.g. Garratt, 1992):

$$F_H = \mu \rho c_p C U\,(T - T_{\mathrm{s}})\,\pi r \sqrt{r^2 + h^2} \tag{9}$$

$$F_L = 0.623 \mu \rho L_{\mathrm{v}} C U p^{-1}\,(e_{\mathrm{s}} - e)\,\pi r \sqrt{r^2 + h^2}. \tag{10}$$

Here C is the bulk turbulent exchange coefficient over a flat surface, T is the air temperature, T_{s} is the surface temperature (set to the melting point), ρ is air density, L_{v} is the latent heat of sublimation (2 830 000 J kg^{-1}), c_p is the specific heat capacity of air (1004 J kg^{-1} K^{-1}), e is the vapour pressure, e_{s} is the saturation vapour pressure, p is atmospheric pressure, and U is the wind speed. The total turbulent heat flux H is just the sum of the fluxes of sensible and latent heat.

The dimensionless parameter μ is an "exposure/roughness parameter" that deals with the fact that an ice stupa has a rough appearance and forms an obstacle to the wind regime. So μ is expected to be larger than 1 and could perhaps have a value of 2 or more. For a larger shape parameter the exposure will be larger; we therefore use

$$\mu = 1 + s/2. \tag{11}$$

Equation (9) is no more than an educated guess. It is hard to base estimates of this parameter on information in the literature. Many studies have been carried out on the effect of obstacles on atmospheric boundary layer flow (e.g. trees, but also buildings), but always in an ensemble setting, looking at the bulk effect of an ensemble of obstacles. We deal with a case of a single obstacle in open terrain, and we are confident that the roughness of the surface and the exposure will lead to larger turbulent fluxes. Given the uncertainty in the exposure parameter, later on we will present results for different values.

When water availability is unlimited, the mass gain or loss is given by

$$\mathrm{d}M/\mathrm{d}t = (F_{\mathrm{sol}} + F_{\mathrm{lw}} + F_L + F_H)/L_{\mathrm{m}} + F_L/L_{\mathrm{v}}. \tag{12}$$

M is the mass of the ice stupa and L_{m} is the latent heat of melting/fusion (334 000 J kg^{-1}). For typical alpine conditions the last term in Eq. (10) is normally quite small. Since the volume of the ice stupa is simply related to the mass ($V = M/\rho_{\mathrm{ice}}$), the height of the stupa can directly be calculated for a given shape factor (case i) or given radius (case ii).

4 Application to the Oberengadin region, Switzerland

Over the past few years, several ice stupas have been constructed in the Oberengadin, southeast Switzerland. In the winter of 2017/2018 an ice stupa was constructed in the Val Roseg at 2000 m a.s.l. (Fig. 1, maximum height about 12 m). In the winter of 2018/2019 several smaller ice stupas (height about 5 m) were built at a site in the Val Morteratsch at about 1900 m a.s.l. Since February 2021 a test site for ice stupa construction has been in operation at the Diavolezza Talstation at an altitude of 2080 m a.s.l.

To obtain first-order estimates of growth and decay rates for typical climatic conditions in the Oberengadin, we used the energy balance measurements from the automatic weather station on the Vadret da Morteratsch as a proxy for this high alpine region. During the period 1 July 2007–30 September 2012, the AWS on the Vadret da Morteratsch was located at an altitude of about 2280 m a.s.l. and has produced a unique data set without any gaps. The annual melt at the AWS location was between 5 and 7 m of ice. With a focus on the Diavolezza site, which is at an altitude of 2080 m a.s.l., a temperature correction of +1.3 K was applied to the input data (based on a standard atmospheric temperature lapse rate of 0.0065 K m^{-1}). We note that all the locations mentioned above are within a distance of 10 km from each other (interactive map to find locations: https://map.wanderland.ch, last access: 25 June 2021).

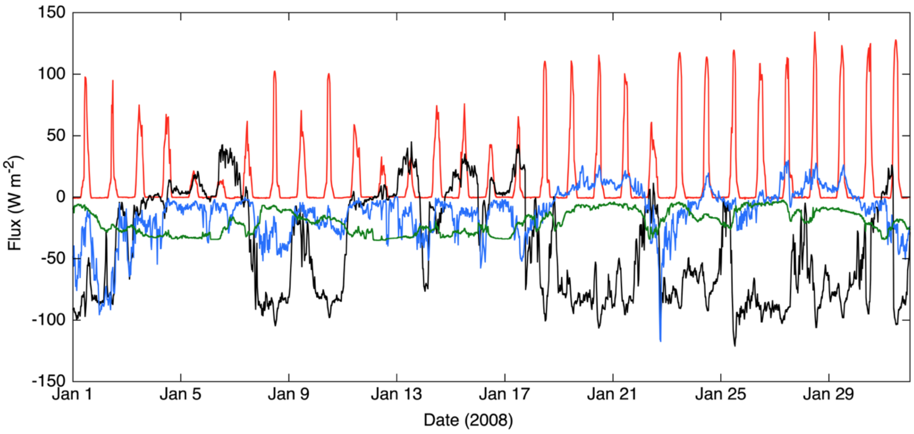

Figure 2. Energy balance components as measured by the AWS on the Vadret da Morteratsch for January 2008. Net solar radiation in red, net longwave radiation flux in black, turbulent sensible heat flux in blue, turbulent latent heat flux in green.

Figure 2 shows an example of data from the AWS. The data have been stored as 30 min averages. The turbulent heat fluxes have been calculated from the wind speed, air temperature, and humidity, where the turbulent exchange coefficient C was used as a tuning parameter (to obtain the correct amount of observed ice melt over a 5-year period). The example shown is just for one relatively sunny winter month (January 2008). Note the large degree of compensation between net solar radiation and net longwave radiation – the well-known effect in clear sky conditions on the radiation balance. As a consequence, the turbulent heat fluxes are more important than it appears at first sight.

Figure 3 summarizes model results in terms of ice stupa height and volume for 5 years. In all calculations we used $q = 0.5$ and $\alpha = 0.6$. It has been assumed that water availability is unlimited. In the first example (Fig. 3a) we show the evolution of an ice stupa on a 5 m high inner structure. In the model this is simply achieved by setting $h = 5$ m at the start of the integration and correct the total volume afterwards for the volume of the inner structure. The use of an inner structure has the advantage that the freezing area is larger from the beginning and that the typical ice stupa shape is achieved relatively fast. The shape factor has been taken constant and equal to 2. We see some differences among the years: the maximum ice stupa height varies between 10 and 12 m and is normally reached in early April. For the last 2 years the simulated ice stupa volume is smaller mainly because of slightly higher temperatures and larger insolation. The decay of the ice stupa is hardly faster than the growth. A faster decay would occur if the albedo were not constant but would be prescribed to decrease during the melt phase (which is more realistic in most cases).

Figure 3b shows a comparison between the fixed-shape simulation just described and a fixed-radius simulation with $r = 7$ m. This value of the radius was chosen to obtain more or less the same ice stupa volume. It can be seen that in the first stage of growth the volume for the fixed-radius case increases somewhat faster than for the fixed-shape case. Nevertheless, the differences in the curves are not large and point to the fact that in the end the energy constraints determine how much ice can form (in the case of unlimited water availability).

Because the value of the exposure parameter μ is highly uncertain, we show the sensitivity of the fixed-radius ice stupa volume to different formulations (Fig. 3c). For $\mu = 1$, implying that the situation is equivalent to that of a flat surface, the stupa volume is significantly smaller than in the reference case ($\mu = 1 + s/2$). A stronger dependence of μ on the shape factor ($\mu = 1 + s$) increases the stupa volume by about 25 %. For a larger shape factor, the mostly negative turbulent fluxes in winter increase, and this is not compensated by a larger interception of solar radiation.

In the simulations discussed so far the ice stupas disappear in summer. One may ask the question under what conditions an ice stupa may survive the summer and grow to a larger size in the next winter. A possible way to study this question is to decrease the air temperature uniformly (temperature change ΔT). This will imply a stronger negative sensible heat flux in winter and a weaker positive heat flux in summer, thus accelerating stupa growth and slowing down its decay. We found a break-even point for $\Delta T \approx -2$ K (Fig. 3d). For larger negative values of ΔT the ice stupa does not disappear in summer and keeps growing from year to year. For $\Delta T \approx -3$ K, the maximum volume in the fifth year ($\sim 2400\,\mathrm{m}^3$) is about 4 times that in the first year ($\sim 600\,\mathrm{m}^3$). We note that in this calculation the effect of lower temperatures on the net longwave radiation balance has not been taken into account, because the radiation fluxes were prescribed according to the AWS observations. It is likely that we therefore underestimate the effect of lower air temperature.

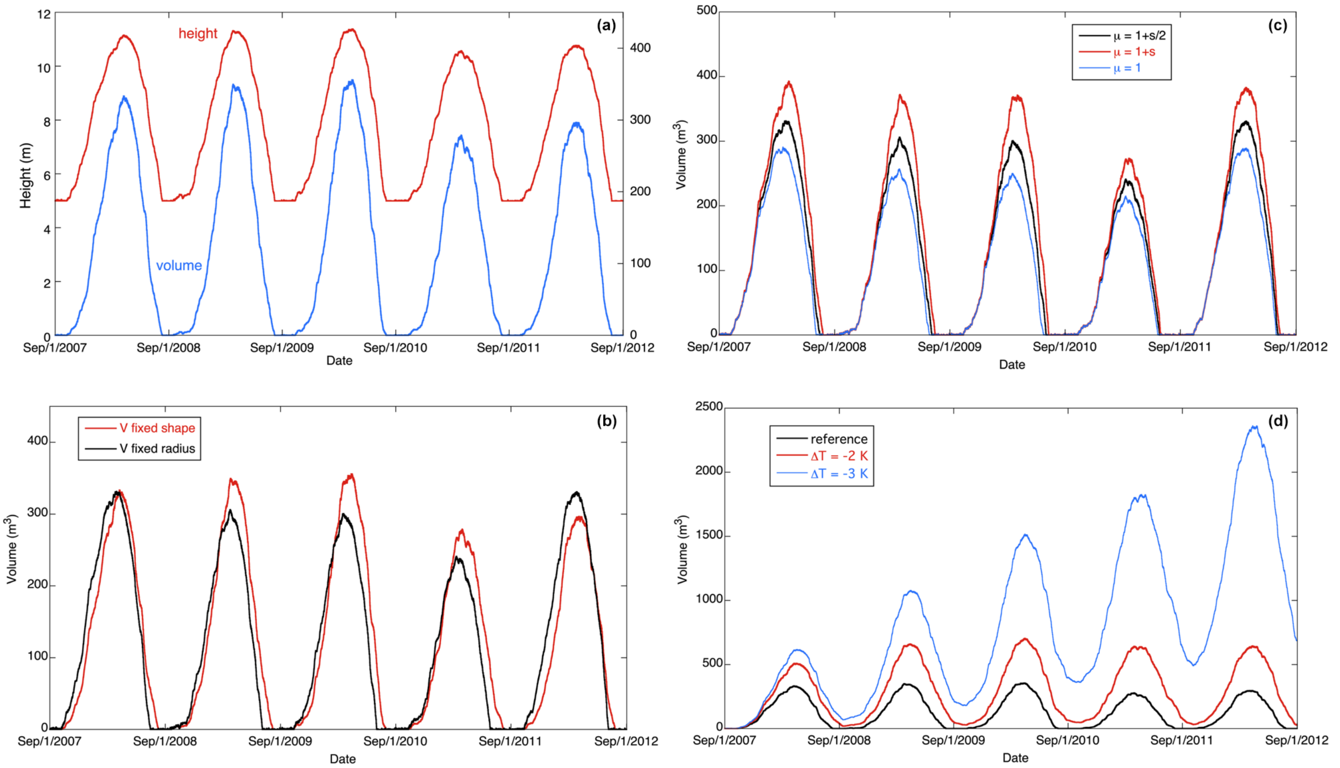

Figure 3. Calculated evolution of ice stupa for the case of unlimited water supply for five winters. **(a)** Height and volume for the case with an inner structure (height 5 m) and fixed shape. **(b)** Volume for the case with an inner structure and the case with a fixed radius (7 m). **(c)** The effect of the exposure parameter μ on the volume (fixed radius). **(d)** The effect of a negative temperature perturbation. For $\Delta T = -3$ K the stupa does not disappear anymore but is growing from year to year (fixed shape).

5 Discussion

The data set used to simulate ice stupa growth and decay for typical conditions in the Oberengadin is probably quite appropriate. The setting of the location of the AWS (on the lower tongue of the Vadret da Morteratsch when it still existed) and the Diavolezza Talstation are rather similar: the altitude is about the same, and the valley is relatively wide. However, differences in the wind statistics are likely to exist, but they are difficult to assess. The Morteratsch AWS reveals a steady katabatic (glacier) wind most of the time, whereas the Diavolezza Talstation is more exposed to the larger-scale wind regime. It seems likely that the average wind speed at the Diavolezza Talstation is somewhat higher than at the AWS site, where the 5-year average wind speed is 2.8 m s^{-1}. In contrast, the sites in the Val Roseg and Val Morteratsch are more sheltered and wind speeds are probably lower.

The examples presented here are best-case scenarios with respect to ice stupa growth. In practice it is not always possible to have unlimited water availability, and it may be difficult to sprinkle the water more or less evenly over the stupa, especially at higher wind speeds. The choice of the shape of the ice stupa depends on the sprinkling strategy. It may be more realistic to describe an ice stupa with different shapes for the growth phase (e.g. fixed radius) and decay phase (e.g. constant shape factor). Such an approach can easily be accommodated in the model.

We note that the ice stupa volume calculated here for alpine conditions at ~2100 m a.s.l. (typically 250 m^3) is significantly smaller than the volumes obtained in the big ice stupas in Ladakh. Winter conditions in Ladakh are considerably colder and therefore growth rates can be much larger.

In this exploratory study a solid comparison between observed and simulated stupa sizes was not attempted. However, we note that the maximum height of the stupa in the Val Roseg was 12 m, which is in good agreement with the stupa height shown in Fig. 3a.

The model presented here is simple, basically because we consider the ice stupa to be a single unit with a surface temperature close to the melting point. As soon as this constraint is relaxed and the surface temperature of the stupa is considered to be a dependent variable, the whole procedure becomes more complicated, and some processes can be studied more explicitly. Nevertheless, we believe that the simple approach presented in this note, which requires no more than one page of coding, is a useful tool to obtain first-order estimates of growth and decay rates under various conditions. Effects of snow cover, switching off water during daytime, switching of water supply for high wind speeds, different starting dates, differences between warm and cold winters, etc. can be evaluated. We finally note that the model can easily be reformulated for another geometry, e.g. a dome.

Data availability. The 5-year data set from the weather station on the Vadret da Morteratsch is available on request.

Author contributions. JO designed, coded, and ran the model. Through their experience in constructing ice stupas, SB, CC, and FK have made important contributions concerning the concept and application of the model. JO wrote the text of this communication.

Competing interests. The authors declare that they have no conflict of interest.

Disclaimer. Publisher's note: Copernicus Publications remains neutral with regard to jurisdictional claims in published maps and institutional affiliations.

Acknowledgements. We thank the reviewers and editor for their constructive comments. The operation of the weather station on the Vadret da Morteratsch was made possible by the NWO-SPINOZA grant (Dutch Research Council) to Johannes Oerlemans.

Review statement. This paper was edited by Chris Derksen and reviewed by Jonathan D. Mackay and two anonymous referees.

References

Berrizbeitia, S. E., Cago, E. J., and Muneer, T.: Empirical models of the estimation of solar sky-diffusive radiation. A review and experimental analysis, Energies, 13, 701, https://doi.org/10.3390/en13030701, 2020.

Garratt, J.: The Atmospheric Boundary Layer, Cambridge University Press, 316 pp., ISBN 0521380529, 1992.

Li, D. H. W., Lou, S. W., and Lam, J. C.: An analysis of global, direct and diffuse solar radiation, Energy Procedia, 75, 388–393, 2015.

Nüsser, M., Dame, J., Kraus, B., Baghel, R., and Schmidt, S.: Socio-hydrology of artificial glaciers in Ladakh, India: assessing adaptive strategies in a changing cryosphere, Reg. Environ. Change, 19, 1327–1337, https://doi.org/10.1007/s10113-018-1372-0, 2018.

Oerlemans, J., Giesen, R. H., and Van den Broeke, M. R.: Retreating alpine glaciers: increased melt rates due to accumulation of dust (Vadret da Morteratsch, Switzerland), J. Glaciol., 55, 729–736, 2009.

frontiers in Earth Science

ORIGINAL RESEARCH
published: 23 February 2022
doi: 10.3389/feart.2021.771342

Influence of Meteorological Conditions on Artificial Ice Reservoir (Icestupa) Evolution

Suryanarayanan Balasubramanian[1,2]*, Martin Hoelzle[1], Michael Lehning[3], Jordi Bolibar[4], Sonam Wangchuk[2], Johannes Oerlemans[4] and Felix Keller[5,6]

[1]Department of Geosciences, University of Fribourg, Fribourg, Switzerland, [2]Himalayan Institute of Alternatives Ladakh, Leh, India, [3]WSL Institute for Snow and Avalanche Research, Davos, Switzerland, [4]Institute for Marine and Atmospheric Research, Utrecht University, Utrecht, Netherlands, [5]Academia Engiadina, Samedan, Switzerland, [6]ETH, Zürich, Switzerland

Since 2014, mountain communities in Ladakh, India have been constructing dozens of Artificial Ice Reservoirs (AIRs) by spraying water through fountain systems every winter. The meltwater from these structures is crucial to meet irrigation water demands during spring. However, there is a large variability associated with this water supply due to the local weather influences at the chosen location. This study compared the ice volume evolution of an AIR built in Ladakh, India with two others built in Guttannen, Switzerland using a surface energy balance model. Model input consisted of meteorological data in conjunction with fountain discharge rate (mass input of an AIR). Model calibration and validation were completed using ice volume and surface area measurements taken from several drone surveys. The model was successful in estimating the observed ice volume evolution with a root mean square error within 18% of the maximum ice volume for all the AIRs. The location in Ladakh had a maximum ice volume four times larger compared to the Guttannen site. However, the corresponding water losses for all the AIRs were more than three-quarters of the total fountain discharge due to high fountain wastewater. Drier and colder locations in relatively cloud-free regions are expected to produce long-lasting AIRs with higher maximum ice volumes. This is a promising result for dry mountain regions, where AIR technology could provide a relatively affordable and sustainable strategy to mitigate climate change induced water stress.

Keywords: icestupa, water storage, climate change adaptation, geoengineering, energy balance (EB) model, water resource management, Ladakh

OPEN ACCESS

Edited by:
Thomas Vikhamar Schuler, University of Oslo, Norway

Reviewed by:
Alan Rempel, University of Oregon, United States
Lukas U. Arenson, BGC Engineering, Canada

****Correspondence:***
Suryanarayanan Balasubramanian
suryanarayanan.balasubramanian@unifr.ch

Specialty section:
This article was submitted to Cryospheric Sciences, a section of the journal Frontiers in Earth Science

Received: *06 September 2021*
Accepted: *23 December 2021*
Published: *23 February 2022*

Citation:
Balasubramanian S, Hoelzle M, Lehning M, Bolibar J, Wangchuk S, Oerlemans J and Keller F (2022) Influence of Meteorological Conditions on Artificial Ice Reservoir (Icestupa) Evolution. Front. Earth Sci. 9:771342. doi: 10.3389/feart.2021.771342

1 INTRODUCTION

Seasonal snow cover and glaciers are expected to change their water storage capacity due to climate change with major consequences for downriver water supply (Immerzeel et al., 2019). The challenges brought about by these changes are especially important for dry mountain environments such as in Central Asia or the Andes, which directly rely on the seasonal meltwater for their farming and drinking needs (Unger-Shayesteh et al., 2013; Chen et al., 2016; Buytaert et al., 2017; Apel et al., 2018; Hoelzle et al., 2019).

Ladakh, sandwiched between the Himalayan ranges and the Karakoram in India, is one such region experiencing climate change induced water stress. Glaciers in the Ladakh region are vital for sustaining agricultural activities which form the basis for regional food security and socio-economic

FIGURE 1 | Icestupa in Ladakh, India on March 2017 was 24 m tall and contained around 3,700 m^3 of water. Picture Credits: Lobzang Dadul.

development (Labbal, 2000; Schmidt and Nüsser, 2012). During a low precipitation year, glaciermelt and snowmelt are the only sources of water supply to the region (Thayyen and Gergan, 2010). Some villages in Ladakh have already been forced to relocate due to glacial retreat and the corresponding loss of their main fresh water resources (Grossman, 2015).

Around 26 villages in this region (Wangchuk, 2021) have been using artificial ice reservoirs (AIR) to adapt to these changes since they require very little infrastructure, skills and energy to be constructed in comparison to other water storage technologies (Nüsser et al., 2019b; Hock et al., 2019). An AIR is a human-made ice structure typically constructed during the cold winter months and designed to slowly release freshwater during the warm spring and summer months. The main purpose of AIRs is irrigation. Therefore, AIRs are designed to store water in the form of ice as long into the summer as possible. The energy required to construct an AIR is usually derived from the gravitational head of the source water body. Some are constructed horizontally by freezing water using a series of checkdams while others are built vertically by spraying water through fountain systems (Nüsser et al., 2019a). The latter are colloquially referred to as Icestupas and are the subject of this study.

A typical AIR (see **Figure 1**) simply requires a fountain nozzle mounted on a supply pipeline. The water source is usually a high altitude lake or glacial stream. Due to the altitude difference between the pipeline input and fountain output, water ejects from the fountain nozzle as droplets which freeze under subzero winter conditions. The fountain is manually activated during winter nights. The fountain nozzle is raised through the addition of metal pipes when significant ice accumulates below. Typically, a dome of branches is constructed around the metal pipes so that pipe extensions can be done from within this dome. Threads, tree branches and fishing nets are used to guide and accelerate the ice formation.

However, to date, no reliable estimates exist about the quantity of meltwater an AIR can provide (Nüsser et al., 2019a). Moreover, preliminary estimates of AIRs in Ladakh indicate that they generate high water losses during their lifetimes (see **Supplementary Appendix 7.1**). During their accumulation period, AIRs can lose excessive fountain water and, during the ablation period, sublimation losses could also be significant. However, the relative contribution of these processes in the total water loss remains unknown.

In this paper, we develop a physically-based model of vertical AIRs (or Icestupas) that can estimate their freezing and melting rates. Mass and energy balance equations were used to estimate the quantity of ice, meltwater, sublimation and wastewater. Sensitivity and uncertainty analysis were performed to identify the most sensitive parameters and the variance they caused. For calibration, we chose two AIRs built across the winter of 2020/21 in India and Switzerland, and validated the model on a Swiss AIR built during winter 2019/20. Our model results provide a first step towards evaluating the potential of this decade old water storage technology worldwide (Wangchuk, 2014).

2 STUDY SITES AND DATA

The model requires three kinds of datasets containing weather, fountain and AIR volume measurements to accurately calibrate, estimate and validate the ice volume of AIRs. Through the winters of 2018/19, 2019/20 and 2020/21, such datasets were acquired for four AIRs in both Switzerland and India. Here, we present the results of three AIRs, which have a complete dataset. Two of them were constructed in the same Swiss location called Guttannen (referred to with the prefix CH) but during different winters, and the other was constructed at Gangles, India (referred to with the prefix IN). The 2020/21 AIR constructed on both these locations are shown in **Figure 2**.

The Guttannen site (46.66 °N, 8.29 °E) in the Bern region lies at 1047 m a.s.l.. In the winter (Oct-Apr), mean daily minimum and maximum air temperatures vary between -13 and 15 °C. Clear skies are rare, averaging around 7 days during winter. Daily winter precipitation can sometimes be as high as 100 mm. These values are based on 30 years of hourly weather model simulations (Meteoblue, 2021). The site was situated adjacent to a stream resulting in high humidity values across the study period as shown in **Figure 2**. AIR were constructed here by the Guttannen Bewegt Association during the winters of 2019–20 (CH20) and 2020–21 (CH21). Tree branches were laid covering the fountain pipe to initiate the ice formation process. The fountain height varied between 2 and 5 m during the construction period. The water was transferred from a spring water source and flowed via a flowmeter to the nozzle. In addition, a webcam guaranteed a continuous survey of the site during the construction of the AIR.

The Gangles site (34.22 °N, 77.61 °E) is located around 20 km north of Leh city in the Ladakh region, lying at 4025 m a.s.l.. The mean annual temperature is 5.6 °C, and the thermal range is characterized by high seasonal variation. During January, the coldest month, the mean temperature drops to − 7.2 °C. During August, the warmest month, the mean temperature rises to

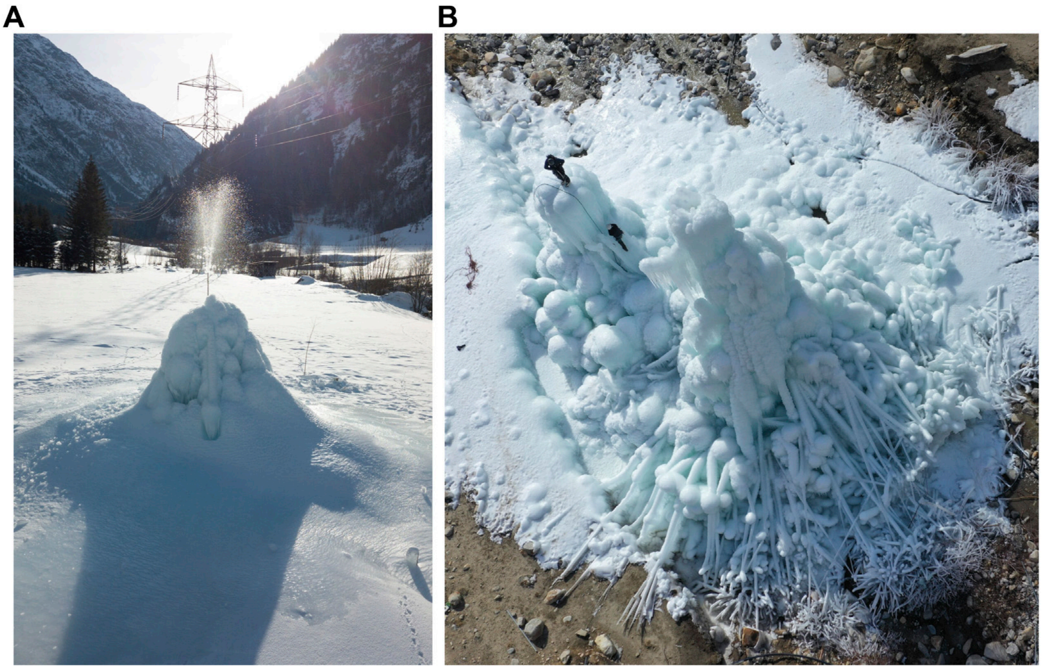

FIGURE 2 | The Swiss and Indian AIRs were 5 m and 13 m tall on January 9 and March 3, 2021 respectively. Picture credits: Daniel Bürki **(A)** and Thinles Norboo **(B)**.

TABLE 1 | Summary of the weather and fountain observations. The expiry date refers to the date when all of the ice of the AIR completely disappeared and only the dome volume remains. The weather measurements are shown using their mean (μ) and standard deviation (σ) during the study period as $\mu \pm \sigma$.

	Name	Symbol	IN21	CH21	CH20	Units
Weather	Air temperature	T_a	0 ± 7	2 ± 6	2 ± 4	$^{\circ}C$
	Relative humidity	RH	35 ± 20	79 ± 18	77 ± 17	%
	Wind speed	v_a	3 ± 1	2 ± 2	2 ± 2	m/s
	Direct Shortwave	SW_{direct}	246 ± 333	80 ± 156	80 ± 150	$W\,m^{-2}$
	Diffuse Shortwave	$SW_{diffuse}$	0 ± 0	58 ± 87	51 ± 74	$W\,m^{-2}$
	Incoming Longwave Radiation	LW_{in}	194 ± 31	239 ± 35	236 ± 34	$W\,m^{-2}$
	Hourly Precipitation	ppt	0 ± 0	139 ± 457	95 ± 404	mm
	Pressure	p_a	623 ± 3	794 ± 9	798 ± 7	hPa
	Start Date		Jan 18 2021	Nov 22 2020	Jan 3 2020	
	Expiry Date		June 20 2021	May 10 2021	April 6 2020	
Fountain	Discharge rate	d_F	60	7.5	7.5	l/min
	Runtime	t_F	829	2155	1553	$hours$
	Spray radius	r_F	10.2	6.9	7.7	m
	Water temperature	T_F	1.5	1.5	1.5	$^{\circ}C$

17.5 $^{\circ}C$ (Nüsser et al., 2012). Because of the rain shadow effect of the Himalayan Range, the mean annual precipitation in Leh totals less than 100 mm, and there is high interannual variability. Whereas the average summer rainfall between July and September reaches 37.5 mm, the average winter precipitation between January and March amounts to 27.3 mm and falls almost entirely as snow. AIRs were constructed here as part of the Ice Stupa Competition by the Himalayan Institute of Alternatives, Ladakh (HIAL). The fountain height of the AIR varied between 5 and 9 m.

2.1 Meteorological Data

Air temperature, relative humidity, wind speed, pressure, longwave, shortwave direct and diffuse radiation are required to calculate the surface energy balance of an AIR (see **Table 1**). The study period starts when the fountain was first switched on and ends when the respective AIR melted completely. These two dates are denoted as start and expiry dates henceforth.

For the CH site, the primary weather data source was a meteoswiss AWS located 184 m away (Station ID: 0–756-0-GTT). In addition, we used ERA5 reanalysis dataset

TABLE 2 | Summary of the drone surveys.

	No.	Date	Volume (m^3)	Radius (m)	Surface Area (m^2)
IN21	1	Jan 18, 2021	103	9.1	411
	2	Feb 27, 2021	580	10.2	668
	3	Mar 3, 2021	626	10.3	694
	4	Mar 15, 2021	692	10	681
	5	Mar 26, 2021	582	10.2	671
	6	Apr 3, 2021	620	10.1	658
CH21	1	Nov 22, 2020	13	5.4	136
	2	Dec 2, 2020	26	5.7	118
	3	Dec 30, 2020	43	7.5	189
	4	Jan 9, 2021	82	6.5	150
	5	Mar 6, 2021	108	7.5	183
	6	Apr 2, 2021	83	6.5	150
	7	Apr 16, 2021	64	6.2	134
	8	Apr 24, 2021	37	4.7	80
CH20	1	Jan 3, 2020	24	6.7	170
	2	Jan 24, 2020	59	7.7	228

(Copernicus Climate Change Service (C3S), 2017) for filling data gaps and adding the shortwave and longwave radiation data that were not measured directly. The ERA5 reanalysis dataset is known to have a high correlation with sites in Switzerland (Scherrer, 2020). The Guttannen temperature dataset had a correlation greater than 0.8 with the ERA5 temperature for both winters. The ERA5 grid point chosen (46.64 °N, 8.25 °E) for the Swiss site was around 3.6 km away from the actual site. ERA5 variables (except incoming shortwave and longwave radiation) were fitted to the meteoswiss dataset via linear regressions. The zero wind speed values recorded by the meteoswiss AWS whenever snow accumulated on the ultrasonic wind sensor were replaced using the ERA5 dataset.

For the IN site, two different weather data sources were used to log all weather parameters required for the model. Temperature, humidity, wind speed and pressure data were logged with a weather station located 440 m away from the construction site. Shortwave radiation data were derived from another weather station located 15 km away. Unfortunately, precipitation was not logged. Since winter precipitation in Ladakh is less than 30 mm (Nüsser et al., 2012), we can safely assume negligible precipitation and mostly clear skies. As a consequence, the diffuse fraction of the global shortwave radiation was also assumed to be negligible. Temperature and humidity were measured with a rotronic sensor with an accuracy of ± 0.3 $^{\circ}C$ and ± 1% respectively. A young sensor measured the wind speed with an accuracy of ± 0.3 ms^{-1} and a setra sensor measured the pressure with an accuracy of ± 0.01 hPa.

2.2 Fountain Observations

We define the fountain used through four attributes; namely, its spray radius, mean discharge rate, discharge runtime and water temperature as shown in **Table 1**. Continuous measurement of the discharge rate was unsuccessful in all sites due to data logger malfunctions of the associated flowmeter. Instead the discharge duration was first determined and then the available discharge measurement was used to determine the average discharge rate d_F during these periods. The spray radius r_F was estimated from the mean AIR circumference measured in the drone surveys during the fountain runtime.

The Swiss fountain discharge duration was extrapolated from just one fountain on and off event each. Even though the Indian fountain was never manually switched off, there were many pipeline freezing events that interrupted the discharge duration. Discharge rate was extrapolated to be the mean discharge rate d_F except during these pipeline freezing events.

2.3 Drone Surveys

Several photogrammetric surveys using drones were conducted on the Swiss and Indian sites. The details of these surveys and the methodology used to produce the corresponding outputs are explained in **Supplementary Appendix 7.2**. The digital elevation maps (DEMs) generated from the obtained imagery were analysed to document the radius, surface area and volume of the ice structure. The number of surveys conducted for the IN21, CH21 and CH20 AIRs were six, eight and two, respectively (see **Table 2**). The first drone flight was used to set the dome volume (V_{dome}) for model initialisation. The remaining surveys were used for model calibration and validation. Since the Indian AIR was built on top of another ice structure (see **Figure 2**), it had a much higher dome volume compared to the other AIRs.

3 MODEL SETUP

A bulk energy and mass balance model is used to calculate the amounts of ice, meltwater, water vapour and wastewater of the AIR. In each hourly time step, the model uses the AIR surface area, energy balance and mass balance calculations to estimate its ice volume, surface temperature and wastewater as shown in **Figure 3** .

3.1 Surface Area Calculation

The model assumes the AIR shape to be a cone and assigns the following shape attributes:

$$A^i_{cone} = \pi \cdot r^i_{cone} \cdot \sqrt{(r^i_{cone})^2 + (h^i_{cone})^2} \quad (1a)$$

$$V^i_{cone} = \pi/3 \cdot (r^i_{cone})^2 \cdot h^i_{cone} \quad (1b)$$

$$j^i_{cone} = \frac{\Delta M^i_{ice}}{\rho_{water} * A^i_{cone}} \quad (1c)$$

where i denotes the model time step, r^i_{cone} is the radius; h^i_{cone} is the height; A^i_{cone} is the surface area; V^i_{cone} is the volume and j^i_{cone} is the AIR surface normal thickness change as shown in **Figure 4**. M^i_{ice} is the mass of the AIR and $\Delta M^i_{ice} = M^{i-1}_{ice} - M^{i-2}_{ice}$. Henceforth, the equations used display the model time step superscript i only if it is different from the current time step.

AIR volume can also be expressed as:

$$V_{cone} = \frac{M_{ice}}{\rho_{ice}} \quad (2)$$

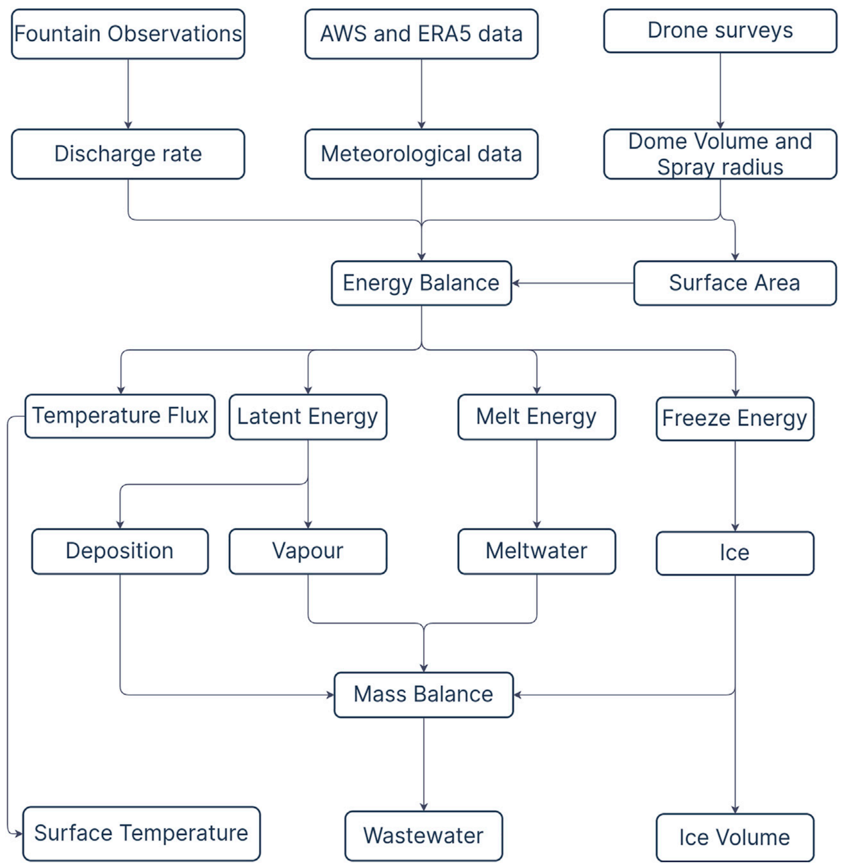

FIGURE 3 | Model schematic showing the workflow used in the model at every time step.

where ρ_{ice} is the density of ice (917 kg m^{-3}).

The initial radius of the AIR is assumed to be r_F. The initial height h_0 depends on the dome volume V_{dome} used to construct the AIR as follows:

$$h_0 = \Delta x + \frac{3 \cdot V_{dome}}{\pi \cdot (r_F)^2} \tag{3}$$

where Δx is the surface layer thickness (defined in **Section 3.2**)

During the subsequent time steps, the dimensions of the AIR evolve assuming a uniform thickness change (j_{cone}) across its surface area with an invariant slope $s_{cone} = \frac{h_{cone}}{r_{cone}}$. During these time steps, the volume is parameterised using **Eq. 1b** as:

$$V_{cone} = \frac{\pi \cdot (r_{cone})^3 \cdot s_{cone}}{3} \tag{4}$$

We define the Icestupa boundary through its spray radius, i.e. we assume ice formation is negligible when $r_{cone} > r_F$. Combining **Eqs 1b**, **2 Eqs 3**, **4**, **4**, the geometric evolution of the Icestupa at each time step i can be determined by considering the following rules:

$$(r_{cone}, h_{cone}) = \begin{cases} (r_F, h_0) & if \;\; i = 0 \\ \left(r_{cone}^{i-1}, \dfrac{3 \cdot M_{ice}}{\pi \cdot \rho_{ice} \cdot (r_{cone}^{i-1})^2} \right) & if \;\; r_{cone}^{i-1} \geq r_F \; and \; \Delta M_{ice} > 0 \\ \left(\dfrac{3 \cdot M_{ice}}{\pi \cdot \rho_{ice} \cdot s_{cone}} \right)^{1/3} \cdot (1, s_{cone}) & otherwise \end{cases} \tag{5}$$

3.2 Energy Balance Calculation

We approximate the energy balance at the surface of an AIR by a one-dimensional description of energy fluxes into and out of a (thin) layer with thickness Δx:

$$\rho_{ice} \cdot c_{ice} \cdot \frac{\Delta T}{\Delta t} \cdot \Delta x = q_{SW} + q_{LW} + q_L + q_S + q_F + q_G \tag{6}$$

Upward and downward fluxes relative to the ice surface are positive and negative, respectively. The first term is the energy change of the surface layer, which can be translated into a phase change energy should phase changes occur; q_{SW} is the net shortwave radiation; q_{LW} is the net longwave radiation; q_L and q_S are the turbulent latent and sensible heat fluxes. q_F represents the heat exchange of the fountain water droplets with the AIR ice surface. q_G represents ground heat flux between the AIR surface and its interior.

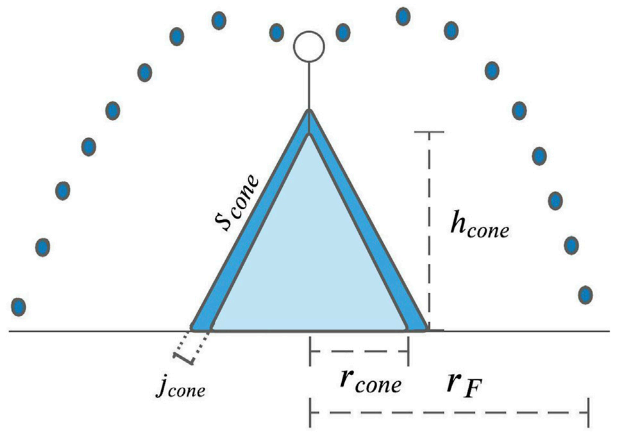

FIGURE 4 | Shape variables of the AIR. r_{cone} is the radius, h_{cone} is the height, j_{cone} is the thickness change and s_{cone} is the slope of the ice cone. r_F is the spray radius of the fountain.

The energy flux acts upon the AIR surface layer, which has an upper and lower boundary defined by the atmosphere and the ice body of the AIR, respectively. A sensitivity analysis was later performed to understand the influence of this factor and decide its value. Here, we define the surface temperature T_{ice} to be the modelled average temperature of the icestupa surface layer.

3.2.1 Net Shortwave Radiation q_{SW}

The net shortwave radiation q_{SW} is computed as follows:

$$q_{SW} = (1 - \alpha) \cdot (SW_{direct} \cdot f_{cone} + SW_{diffuse}) \tag{7}$$

where SW_{direct} and $SW_{diffuse}$ are the direct and diffuse shortwave radiation, α is the modelled albedo and f_{cone} is the area fraction of the ice structure exposed to the direct shortwave radiation.

The albedo varies depending on the water source that formed the current AIR surface layer. During the fountain runtime, the albedo assumes a constant value corresponding to ice albedo. However, after the fountain is switched off, the albedo can reset to snow albedo during snowfall events and then decay back to ice albedo. We use the scheme described in Oerlemans and Knap (1998) to model this process. The scheme records the decay of albedo with time after fresh snow is deposited on the surface. δt records the number of time steps after the last snowfall event. After snowfall, albedo changes over a time step, δt , as

$$\alpha = \alpha_{ice} + (\alpha_{snow} - \alpha_{ice}) \cdot e^{(-\delta t)/\tau} \tag{8}$$

where α_{ice} is the bare ice albedo value (0.25), α_{snow} is the fresh snow albedo value (0.85) and τ is a decay rate (16 *days*), which determines how fast the albedo of the ageing snow recedes back to ice albedo.

The solar area fraction f_{cone} of the ice structure exposed to the direct shortwave radiation depends on the shape considered. Using the solar elevation angle θ_{sun}, the solar beam can be considered to have a vertical component, impinging on the horizontal surface (semicircular base of the AIR), and a horizontal component impinging on the vertical cross section (a triangle). The solar elevation angle θ_{sun} used is modelled using the parametrisation proposed by Woolf (1968). Accordingly, f_{cone} is determined as follows:

$$f_{cone} = \frac{(0.5 \cdot r_{cone} \cdot h_{cone}) \cdot \cos\theta_{sun} + (\pi \cdot (r_{cone})^2/2) \cdot \sin\theta_{sun}}{\pi \cdot r_{cone} \cdot ((r_{cone})^2 + (h_{cone})^2)^{1/2}} \tag{9}$$

The diffuse shortwave radiation is assumed to impact the conical AIR surface uniformly.

3.2.2 Net Longwave Radiation q_{LW}

The net longwave radiation q_{LW} is determined as follows:

$$q_{LW} = LW_{in} - \sigma \cdot \epsilon_{ice} \cdot (T_{ice} + 273.15)^4 \tag{10}$$

where T_{ice} is the modelled surface temperature given in [°C], $\sigma = 5.67 \cdot 10^{-8}$ $Jm^{-2}s^{-1}K^{-4}$ is the Stefan-Boltzmann constant, LW_{in} denotes the incoming longwave radiation and ϵ_{ice} is the corresponding emissivity value for the Icestupa surface (0.97).

The incoming longwave radiation LW_{in} for the Indian site, where no direct measurements were available, is determined as follows:

$$LW_{in} = \sigma \cdot \epsilon_a \cdot (T_a + 273.15)^4 \tag{11}$$

here T_a represents the measured air temperature and ϵ_a denotes the atmospheric emissivity. We approximate the atmospheric emissivity ϵ_a using the equation suggested by Brutsaert (1982), considering air temperature and vapor pressure (**Eqn. 12**). The vapor pressure of air over water and ice was obtained using **Eq. (15)**. The expression defined in Brutsaert (1975) for clear skies (first term in **equation 12**) is extended with the correction for cloudy skies after Brutsaert (1982) as follows:

$$\epsilon_a = 1.24 \cdot \left(\frac{p_{v,w}}{(T_a + 273.15)}\right)^{1/7} \cdot (1 + 0.22 \cdot cld^2) \tag{12}$$

with a cloudiness index cld, ranging from 0 for clear skies to 1 for complete overcast skies. For the Indian site, we assume cloudiness to be negligible.

3.2.3 Turbulent Fluxes

The turbulent sensible q_S and latent heat q_L fluxes are computed with the following expressions proposed by Garratt (1992):

$$q_S = \mu_{cone} \cdot c_a \cdot \rho_a \cdot p_a \Big/ p_{0,a} \cdot \frac{\kappa^2 \cdot v_a \cdot (T_a - T_{ice})}{\left(\ln \frac{h_{AWS}}{z_0}\right)^2} \tag{13}$$

$$q_L = \mu_{cone} \cdot 0.623 \cdot L_s \cdot \rho_a \Big/ p_{0,a} \cdot \frac{\kappa^2 \cdot v_a (p_{v,w} - p_{v,ice})}{\left(\ln \frac{h_{AWS}}{z_0}\right)^2} \tag{14}$$

where h_{AWS} is the measurement height above the ground surface of the AWS (around 2 m for all sites), v_a is the wind speed in [m s^{-1}], c_a is the specific heat of air at constant pressure (1010 J $kg^{-1}K^{-1}$), ρ_a is the air density at standard sea level (1.29 kgm^{-3}), $p_{0,a}$ is the air pressure at standard sea level

(1013 hPa), p_a is the measured air pressure, κ is the von Karman constant (0.4), z_0 is the surface roughness (3 mm) and L_s is the heat of sublimation (2848 $kJ\,kg^{-1}$). The vapor pressure of air with respect to water ($p_{v,w}$) and with respect to ice ($p_{v,ice}$) was obtained using the formulation given in Huang (2018) :

$$p_{v,w} = e^{\frac{\left(34.494-\frac{4924.99}{T_a+237.1}\right)}{(T_a+105)^{1.57}\cdot 100}} \cdot \frac{RH}{100}$$
$$p_{v,ice} = e^{\frac{\left(43.494-\frac{6545.89}{T_{ice}+278}\right)}{(T_{ice}+868)^{2}\cdot 100}} \tag{15}$$

The dimensionless parameter μ_{cone} is an exposure parameter that deals with the fact that AIR has a rough appearance and forms an obstacle to the wind regime. This factor accounts for the larger turbulent fluxes due to the roughness of the surface (Oerlemans et al., 2021), and is a function of the AIR slope as follows:

$$\mu_{cone} = 1 + \frac{s_{cone}}{2} \tag{16}$$

A possible source of error is the fact that wind measurements from the horizontal plane at the AWS are used, which might be different from those on a slope. However, without detailed datasets from the AIR surface, we retain this assumption.

3.2.4 Fountain Discharge Heat Flux q_F

The fountain water, at temperature T_F, is assumed to cool to 0 °C. Thus, the heat flux caused by this process is:

$$q_F = \frac{\Delta M_F \cdot c_{water} \cdot T_F}{\Delta t \cdot A_{cone}} \tag{17}$$

with c_{water} as the specific heat of water (4186 J $kg^{-1}K^{-1}$).

3.2.5 Bulk Icestupa Heat Flux q_G

The bulk Icestupa heat flux q_G corresponds to the ground heat flux in normal soils and is caused by the temperature gradient between the surface layer (T_{ice}) and the ice body (T_{bulk}). It is expressed by using the heat conduction equation as follows:

$$q_G = k_{ice} \cdot \left(T_{bulk} - T_{ice}^{i-1}\right)/l_{cone} \tag{18}$$

where k_{ice} is the thermal conductivity of ice (2.123 $W\,m^{-1}\,K^{-1}$) , T_{bulk} is the mean temperature of the ice body within the icestupa and l_{cone} is the average distance of any point in the surface to any other point in the ice body. T_{bulk} is initialised as 0 °C and later determined from **Eq. 18** as follows:

$$T_{bulk}^{i+1} = T_{bulk} - \left(q_G \cdot A \cdot \Delta t\right)/\left(M_{ice} \cdot c_{ice}\right) \tag{19}$$

Since AIRs typically have conical shapes with $r_{cone} > h_{cone}$, we assume that the center of mass of the cone body is near the base of the fountain. Thus, the distance of every point in the AIR surface layer from the cone body's center of mass is between h_{cone} and r_{cone}. Therefore, we calculate q_G assuming $l_{cone} = (r_{cone} + h_{cone})/2$.

3.2.6 Phase Changes

In this section, the numerical procedures to model phase changes at the surface layer are explained. Let T_{temp} be the calculated surface temperature. Therefore, **Eq. (6)** can be rewritten as:

$$q_{total} = \rho_{ice} \cdot c_{ice} \cdot \frac{(T_{temp} - T_{ice})}{\Delta t} \cdot \Delta x$$

where q_{total} represents the total energy available to be redistributed. Even if the numerical heat transfer solution produces temperatures which are T_{temp} > 0°C, say from intense shortwave radiation, the ice temperature must remain at T_{temp} = 0°C. The "excess" energy is used to drive the melting process. Moreover, the energy input is used to melt the surface ice layer, and not to raise the surface temperature to some unphysical value. Similarly, for freezing to occur, three conditions are required. Firstly, fountain water is present (ΔM_F > 0) and secondly the calculated temperature of the ice, T_{temp}, is below 0°C. However, these two conditions are not sufficient as the latent heat turbulent fluxes can only contribute to temperature fluctuations. Therefore, an additional condition, namely, (q_{total} − q_L) < 0, is required. Depending on the above conditions, the total energy q_{total} can be redistributed for the melting (q_{melt}), freezing (q_{freeze}) and surface temperature change (q_T) processes as follows:

$$q_{total} = \begin{cases} q_{freeze} + q_T & \text{if } \Delta M_F > 0 \text{ and } T_{temp} < 0 \text{ and } (q_{total} - q_L) < 0 \\ q_{melt} + q_T & \text{otherwise} \end{cases} \tag{20}$$

Henceforth, time steps when the total energy is redistributed to the freezing energy are called freezing events and the rest of the time steps are called melting events.

During a freezing event, the AIR surface is assumed to warm to 0°C. The available energy (q_{total} − q_L) is further increased due to this change in surface temperature represented by the energy flux:

$$q_0 = \frac{\rho_{ice} \cdot \Delta x \cdot c_{ice} \cdot T_{ice}^{i-1}}{\Delta t}$$

The available fountain discharge (ΔM_F) may not be sufficient to utilize all the freezing energy. At such times, the additional freezing energy further cools down the surface temperature. Accordingly, the surface energy flux distribution during a freezing event can be represented as:

$$(q_{freeze}, q_T) = \begin{cases} \left(\frac{\Delta M_F \cdot L_f}{A_{cone} \cdot \Delta t}, q_{total} + \frac{\Delta M_F \cdot L_f}{A_{cone} \cdot \Delta t}\right) & \text{if } \Delta M_F \text{ insufficient} \\ (q_{total} - q_L + q_0, q_L - q_0) & \text{otherwise} \end{cases} \tag{21}$$

If T_{temp} > 0°C, then energy is reallocated from q_T to q_{melt} to maintain surface temperature at melting point. The total energy flux distribution during a melting event can be represented as:

$$(q_{melt}, q_T) = \begin{cases} (0, q_{total}) & \text{if } T_{temp} \le 0 \\ \left(\frac{T_{temp} \cdot \rho_{ice} \cdot c_{ice} \cdot \Delta x}{\Delta t}, q_{total} - \frac{T_{temp} \cdot \rho_{ice} \cdot c_{ice} \cdot \Delta x}{\Delta t}\right) & \text{if } T_{temp} > 0 \end{cases} \tag{22}$$

3.3 Mass Balance Calculation

The mass balance equation for an AIR is represented as:

$$\frac{\Delta M_F + \Delta M_{ppt} + \Delta M_{dep}}{\Delta t} = \frac{\Delta M_{ice} + \Delta M_{water} + \Delta M_{sub} + \Delta M_{waste}}{\Delta t} \tag{23}$$

where M_F is the cumulative mass of the fountain discharge; M_{ppt} is the cumulative precipitation; M_{dep} is the cumulative accumulation through water vapour deposition; M_{ice} is the cumulative mass of ice; M_{water} is the cumulative mass of melt water; M_{sub} represents the cumulative water vapor loss by sublimation and M_{waste} represents the fountain wastewater that did not interact with the AIR. The left hand side of **Eq. 23** represents the rate of mass input and the right hand side represents the rate of mass output for an AIR.

Precipitation input is calculated as shown in **Eq. 24b** where ρ_w is the density of water ($1000\ kg\ m^{-3}$), $\Delta ppt/\Delta t$ is the measured precipitation rate in $[m\ s^{-1}]$ and T_{ppt} is the temperature threshold below which precipitation falls as snow. Here, snowfall events were identified using T_{ppt} as $1^\circ C$. Snow mass input is calculated by assuming a uniform deposition over the entire circular footprint of the AIR.

The latent heat flux is used to estimate either the evaporation and condensation processes or sublimation and deposition processes as shown in **Equation (24c)**. During the time steps at which the surface temperature is below $0\ ^\circ C$ only sublimation and deposition can occur, but if the surface temperature reaches $0\ ^\circ C$, evaporation and condensation can also occur. As the differentiation between evaporation and sublimation (and condensation and deposition) when the air temperature reaches $0\ ^\circ C$ is challenging, we assume that negative (positive) latent heat fluxes correspond only to sublimation (deposition), i.e. no evaporation (condensation) is calculated.

Since we have categorized every time step as a freezing or melting event, we can determine the melting/freezing rates and the corresponding meltwater/ice quantities as shown in **Eqs 24e**, **24d**, and **24f**. Having calculated all other mass components, the fountain wastewater generated every time step can be calculated using **Eq. 23**.

$$\frac{\Delta M_F}{\Delta t} = \begin{cases} \frac{60}{\rho_w \cdot \Delta t} \cdot d_F & if\ \ fountain\ is\ on \\ 0 & otherwise \end{cases} \tag{24a}$$

$$\frac{\Delta M_{ppt}}{\Delta t} = \begin{cases} \pi \cdot (r_{cone})^2 \cdot \rho_w \cdot \frac{\Delta ppt}{\Delta t} & if\ \ T_a < T_{ppt} \\ 0 & if\ \ T_a \geq T_{ppt} \end{cases} \tag{24b}$$

$$\left(\frac{\Delta M_{dep}}{\Delta t}, \frac{\Delta M_{sub}}{\Delta t}\right) = \begin{cases} \frac{q_L \cdot A_{cone}}{L_s} \cdot (1, 0) & if\ \ q_L \geq 0 \\ \frac{q_L \cdot A_{cone}}{L_s} \cdot (0, -1) & if\ \ q_L < 0 \end{cases} \tag{24c}$$

$$\frac{\Delta M_{water}}{\Delta t} = \frac{q_{melt} \cdot A_{cone}}{L_f} \tag{24d}$$

$$\frac{\Delta M_{freeze/melt}}{\Delta t} = \frac{q_{freeze/melt} \cdot A_{cone}}{L_f} \tag{24e}$$

$$\frac{\Delta M_{ice}}{\Delta t} = \frac{q_{freeze} \cdot A_{cone}}{L_f} + \frac{\Delta M_{ppt}}{\Delta t} + \frac{\Delta M_{dep}}{\Delta t} - \frac{\Delta M_{sub}}{\Delta t} - \frac{\Delta M_{water}}{\Delta t} \tag{24f}$$

Considering AIRs as water reservoirs, their net water loss can be defined as:

$$Net\ water\ losses = \frac{M_{waste} + M_{sub}}{(M_F + M_{ppt} + M_{dep})} \cdot 100 \tag{25}$$

3.4 Uncertainty Quantification

The uncertainty in the model of estimating ice volumes is caused by three sources, namely, model forcing data, model hyperparameters and model parameters. Model forcing data can further be divided into weather and fountain forcing data. Significant uncertainty exists in the weather forcing data, particularly for all the radiation measurements (SW_{direct}, $SW_{diffuse}$, LW_{in}) since they were taken from ERA5 dataset or an AWS far away from the construction sites. Since no other weather datasets exist for comparison, especially near the IN21 AIR, we are not accounting for uncertainties related to meteorological forcing data in this analysis. Uncertainty in the fountain forcing data arises due to only some fountain parameters listed in **Table 3**. Fountain runtime t_F has no uncertainty for the Swiss AIRs because no interruptions occured during the study period. However, significant uncertainty exists for the IN21 AIR , where the interruptions due to pipeline freezing events happened overnight but this was ignored in this analysis. Fountain spray radius r_F was measured using the drone survey and therefore also doesn't contribute to model uncertainty. The choice of mean discharge rate d_F for both sites was just a best guess, based on few observations made by the flowmeter. So we associate this parameter by a large uncertainty of ± 50 %. For the fountain water temperature T_F, we assumed an upper bound of $3\ ^\circ C$ since it is unlikely for it to have been beyond this range considering winter conditions at all the sites. The model structure introduces uncertainty through the spatial and temporal hyperparameters Δx and Δt. By definition, Δx is directly proportional to Δt. Therefore, we fix the temporal resolution of the model at hourly timesteps and only investigate the uncertainty caused by Δx here. Since the surface layer thickness for an AIR does not resemble to any parameter in the glaciological literature, we attribute a wide range of values for it (from 1 to 10 cm). The model parameters are henceforth called as weather parameters to distinguish them from the fountain forcing parameters. These were fixed within a range based on literature values (see **Table 3**).

The three types of uncertain parameters namely, model hyperparameters (Δx), fountain forcing parameters (d_F, T_F) and weather parameters (ϵ_{ice}, z_0, α_{ice}, α_{snow}, T_{ppt}, τ) are denoted as Q^M, Q^F and Q^W henceforth. Together, these nine parameters cause a large uncertainty in the ice volume estimates. In order to reduce this uncertainty, we perform a global sensitivity analysis with the net water loss as our objective. The objective of this sensitivity analysis was to reduce the dimension of the parameter space by calibrating the parameters with high total-order sensitivities ($S_{T_j} > 0.5$). The methodology to determine S_{T_j} is described in **Supplementary Appendix 7.3**. These sensitive model parameters were calibrated based on the root mean squared error (RMSE) between the drone

TABLE 3 | Free parameters in the model categorised as constant, derived, model hyperparameters, weather and fountain forcing parameters with their respective values/ranges.

Constant parameters	Symbol	Value	Unit	References
Van Karman constant	κ	0.4	dimensionless	Cuffey and Paterson (2010)
Stefan Boltzmann constant	σ	5.67×10^{-8}	$W\,m^{-2}\,K^{-4}$	Cuffey and Paterson (2010)
Air pressure at sea level	$p_{0,a}$	1013	hPa	Mölg and Hardy (2004)
Density of water	ρ_w	1000	$kg\,m^{-3}$	Cuffey and Paterson (2010)
Density of ice	ρ_{ice}	917	$kg\,m^{-3}$	Cuffey and Paterson (2010)
Density of air	ρ_a	1.29	$kg\,m^{-3}$	Mölg and Hardy (2004)
Specific heat of water	c_w	4186	$J\,kg^{-1}\,°C^{-1}$	Cuffey and Paterson (2010)
Specific heat of ice	c_{ice}	2097	$J\,kg^{-1}\,°C^{-1}$	Cuffey and Paterson (2010)
Specific heat of air	c_a	1010	$J\,kg^{-1}\,°C^{-1}$	Mölg and Hardy (2004)
Thermal conductivity of ice	k_{ice}	2.123	$W\,m^{-1}\,K^{-1}$	Bonales et al. (2017)
Latent Heat of Sublimation	L_s	2.85×10^6	$J\,kg^{-1}$	Cuffey and Paterson (2010)
Latent Heat of Fusion	L_f	3.34×10^5	$J\,kg^{-1}$	Cuffey and Paterson (2010)
Gravitational acceleration	g	9.81	$m\,s^{-2}$	Cuffey and Paterson (2010)
Weather station height	h_{AWS}	2	m	assumed
Model timestep	Δt	3600	s	assumed
Fountain spray radius	r_F		m	measured
Fountain runtime	t_F		$hours$	measured
Derived Parameters	**Symbol**		**Unit**	**Section**
Radius of AIR	r_{cone}		m	3.1
Height of AIR	h_{cone}		m	3.1
Slope of AIR	s_{cone}		dimensionless	3.1
Thickness change of AIR	j_{cone}		m	3.1
Atmospheric emissivity	ϵ_a		dimensionless	3.2.2
Cloudiness	cld		dimensionless	assumed
Vapour pressure over water	$p_{v,w}$		hPa	3.2.3
Vapour pressure over ice	$p_{v,ice}$		hPa	3.2.3
Solar elevation angle	θ_{sun}		°	3.2.1
Albedo	α		dimensionless	3.2.1
Solar area fraction	f_{cone}		dimensionless	3.2.1
Ice body and surface distance	l_{cone}		m	3.2.5
AIR surface temperature	T_{ice}		$°C$	3.2.5
AIR bulk temperature	T_{bulk}		$°C$	3.2.5
Model Hyperparameters	**Symbol**	**Range**	**Unit**	**References**
Surface layer thickness	Δx	$[1e-2, 1e-1]$	m	assumed
Weather Parameters	**Symbol**	**Range**	**Unit**	**References**
Ice Emissivity	ϵ_{ice}	[0.95, 0.99]	dimensionless	Hori et al. (2006)
Surface Roughness	z_0	$[1e-3, 5e-3]$	m	Brock et al. (2006)
Ice Albedo	α_{ice}	[0.15, 0.35]	dimensionless	Steiner et al. (2015) Zolles et al. (2019)
Snow Albedo	α_{snow}	[0.8, 0.9]	dimensionless	Zolles et al. (2019)
Precipitation Temperature threshold	T_{ppt}	[0, 2]	$°C$	Zhou et al. (2010)
Albedo Decay Rate	τ	[10, 22]	$days$	Schmidt et al. (2017) Oerlemans and Knap (1998)
Fountain Forcing Parameters	**Symbol**	**Range**	**Unit**	**References**
Discharge rate	d_F	$[0.5 \cdot d_F, 1.5 \cdot d_F]$	$l/\min$	assumed
Water temperature	T_F	[0, 3]	$°C$	assumed

surveys (see **Table 2**) and the model estimations of the ice volume. For this calibration procedure, all the other parameters were set to the median value of their respective ranges defined in **Table 3**. The sensitivity analysis and calibration were carried out with the drone surveys of CH21 and IN21 AIRs.

The model uncertainty was quantified separately for the remaining parameters in Q^M, Q^F and Q^W using the corresponding 90 % prediction interval I^M, I^F and I^W. The 90 % prediction interval, I^k, gives us the interval within which 90 % of the ice volume outcomes occur when all the parameters in Q^k are varied assuming each has an independent uniform probability density function. 5 % of the outcomes are above and 5 % are below this interval. The methodology to obtain this is described in **Supplementary Appendix 7.3**.

For validation, the calibrated model was tested with two datasets namely, the expiry date of all AIRs and the drone surveys of CH20 AIR.

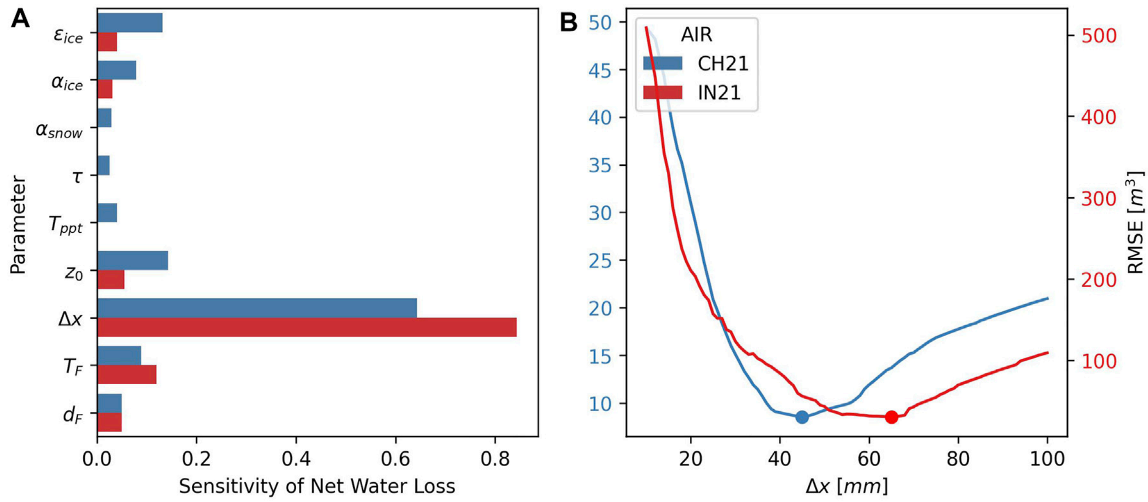

FIGURE 5 | (A) Total-order sensitivities of all the uncertain parameters of the model with net water loss as the objective. **(B)** The calibration of the sensitive parameter, Δx with the RMSE between the drone and model estimates of the ice volume. The dots denote the optimum values. The estimates from the Swiss and Indian AIRs are denoted with blue and red colors respectively.

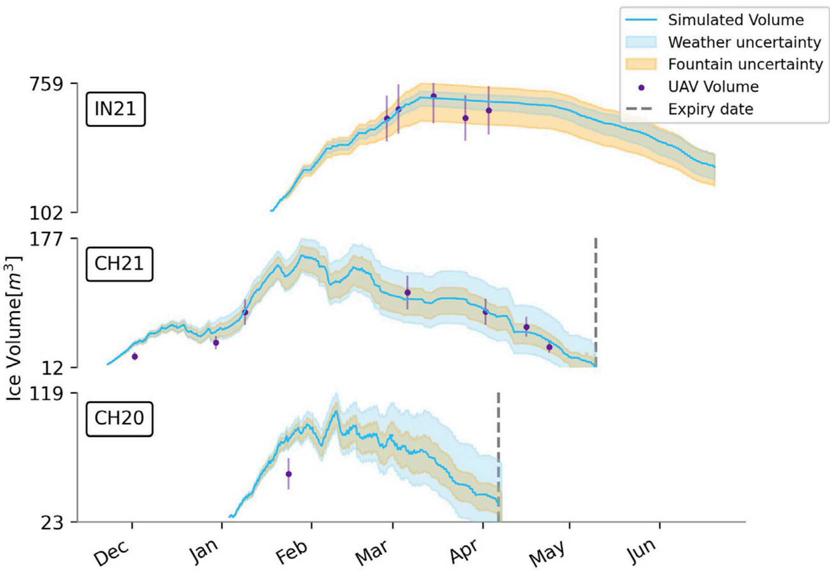

FIGURE 6 | Simulated ice volume during the lifetime of the AIRs (blue curve). The shaded regions (light blue and orange) represent the 90% prediction interval of the AIR ice volume caused by the variations in weather and fountain forcing parameters, respectively. Violet points indicate the drone ice volume observations. The grey dashed line represents the observed expiry date for each AIR.

4 RESULTS

4.1 Calibration of Sensitive Parameters

The total-order sensitivities of all the nine parameters with respect to the net water loss objective are shown in **Figure 5A** . In total, the global sensitivity analysis required 1432 model runs to determine these sensitivities for each site. The only sensitive parameter ($S_{T_j} > 0.5$) for both AIRs was the surface layer thickness. The RMSE between the drone surveys and the model ice volume estimates for different surface layer thickness are shown in **Figure 5B**. The optimum value of Δx was found to be 45 and 65 mm with an RMSE of 9 m^3 and 30 m^3 for CH21 and IN21 AIRs respectively.

4.2 Weather and Fountain Forcing Uncertainty Quantification

The uncertainty in the ice volume estimates caused by the weather and fountain forcing parameters are shown in **Figure 6**. The ranges highlighted represent the corresponding 90 % prediction interval of the ice volume estimates. Weather uncertainty determination required 422 simulations whereas fountain forcing uncertainty determination required 32 simulations for each AIR. Since the results presented below differ significantly during the fountain runtime, we divided the simulation duration of the AIR into accumulation and ablation periods. The accumulation (ablation) period ends (starts) at the last fountain discharge event.

The prediction interval of the weather and fountain forcing parameters behave differently during the accumulation and ablation period for all AIRs. Prediction interval of the weather parameters increase throughout the simulation period, but that of the fountain forcing parameters only increase during the accumulation period. This is to be expected since the fountain forcing parameters directly affect the model estimates only during the accumulation period.

Weather uncertainty for the Indian site was low compared to the Swiss since precipitation and the associated variation in albedo was negligible. At the end of the accumulation period, the Indian weather prediction interval had a magnitude of 73 m^3 which was 10 % of the maximum simulated volume, whereas the magnitude of the Swiss weather prediction interval was much higher (28 % of the maximum simulated volume for the CH21 AIR). This was expected since four out of the six uncertain Indian weather parameters were part of the albedo module. Among all the weather parameters, surface roughness caused the most variance in both Indian and the Swiss ice volume estimates.

Fountain forcing uncertainty for the Indian site was higher than its weather uncertainty (28 % of the maximum simulated volume at the end of the accumulation period). This was predominantly due to the uncertainty in the fountain's water temperature. However, for the Swiss site, the prediction interval of the fountain forcing parameters was similar to that of the weather parameters during the accumulation period. Since the mean fountain discharge rate of the Indian location was eight times that of the Swiss, the uncertainty due to the fountain forcing parameters was expected to be larger for the Indian location.

4.3 Validation

Model performance can be judged based on the ice volume left on the expiry date of all AIRs. In the case of CH21 AIR no ice volume was left whereas for CH20 AIR ice volume of 12 m^3 was left on the expiry date. For the IN21 AIR, the determination of the expiry date was not possible. In reality, the IN21 AIR was found to have disintegrated into several ice blocks on 20th June 2021.

There was also one drone survey of the CH20 AIR volume for validation purposes (see **Table 2**). The RMSE of that observation with the modelled volume was 19 m^3 which is 18 % of the maximum simulated ice volume of CH20 AIR.

4.4 AIR Ice Volume Estimates

Since this model used a surface energy balance model commonly applied on glaciers, we analyse the AIR temporal and spatial variation similar to how it is done for a glacier. Particularly, we used the AIR surface normal thickness change (j_{cone}) as a measure to quantify the location influence. Note that j_{cone} is similar to the "specific mass balance" of a glacier with units *m w. e*. The thickness change during the accumulation and ablation period was referred to as thickness growth and decay, respectively.

The construction decisions responsible for the observed magnitude and variance of the ice volume estimates can be categorised based on the fountain used and the location selected. According to **Eq. 24e**, the freezing/melting rate of the AIRs can be decomposed to the corresponding freezing/melting energy and the surface area. The construction location chosen determines the thickness growth/decay through the freezing/melting energy flux and the fountain determines the surface area through its spray radius.

The influence of location can be further comprehended if we analyse the daily surface normal thickness change together with the corresponding energy fluxes. **Figure 7** shows the daily thickness and energy balance components calculated with the calibrated surface layer thickness for the first and last 20 days for each AIR. The two time periods selected were characteristic of the accumulation and ablation period, respectively. A strong variability was evident between the accumulation and ablation periods and between the CH21 and the IN21 AIRs.

The daily mean thickness change of the Indian location was positive (3 *mm w.e.*) with a daily mean growth of 31 *mm w.e.* and a mean decay of 11 *mm w.e.* In the Swiss location, the daily mean thickness change was negative ($-$ 4 *mm w.e.*) with a daily mean thickness growth of 8 *mm w.e.* and a mean decay of 18 *mm w.e.* The difference in magnitude between the growth and the decay corresponds to the difference between the freezing and the melting energy balance components. For the Indian site, q_{freeze} accounted for 73 %, q_{melt} accounted for 23 % and q_T just 4 % of overall energy turnover. The energy turnover is calculated as the sum of energy fluxes in absolute values. For the Swiss site, q_{freeze} accounted for 37 %, q_{melt} accounted for 61 % and q_T just 2 % of overall energy turnover. The freezing events occurred for 19 and 34% of the simulation duration (see **Table 1**) for the Indian and Swiss sites, respectively. The accumulation period is characteristic of these freezing events and the ablation period is characteristic of the melting events. We compare the energy turnover of different energy fluxes between these two periods to quantify the influence of different surface processes.

To understand the overall impact of the radiation fluxes (longwave and shortwave) and the turbulent fluxes (sensible and latent) on the freezing and melting energies, we sum their respective energy turnover by taking into account the sign of their mean energy during the accumulation/ablation period (see **Table 4**). A negative sign indicates that the corresponding energy flux increased/decreased the freezing/melting energy respectively. Note that all energy fluxes maintain the same sign for both accumulation and ablation periods for the Indian location, but the latent heat changes sign for the Swiss location. The radiation fluxes contributed -27 and 0 % to the freezing and melting energies for the Indian location and -20 % and -6 % to the Swiss location, respectively. Similarly, the turbulent fluxes at the Indian location contribute -11 and 10 % and at the Swiss location contribute 12 and 49% respectively. Therefore, the

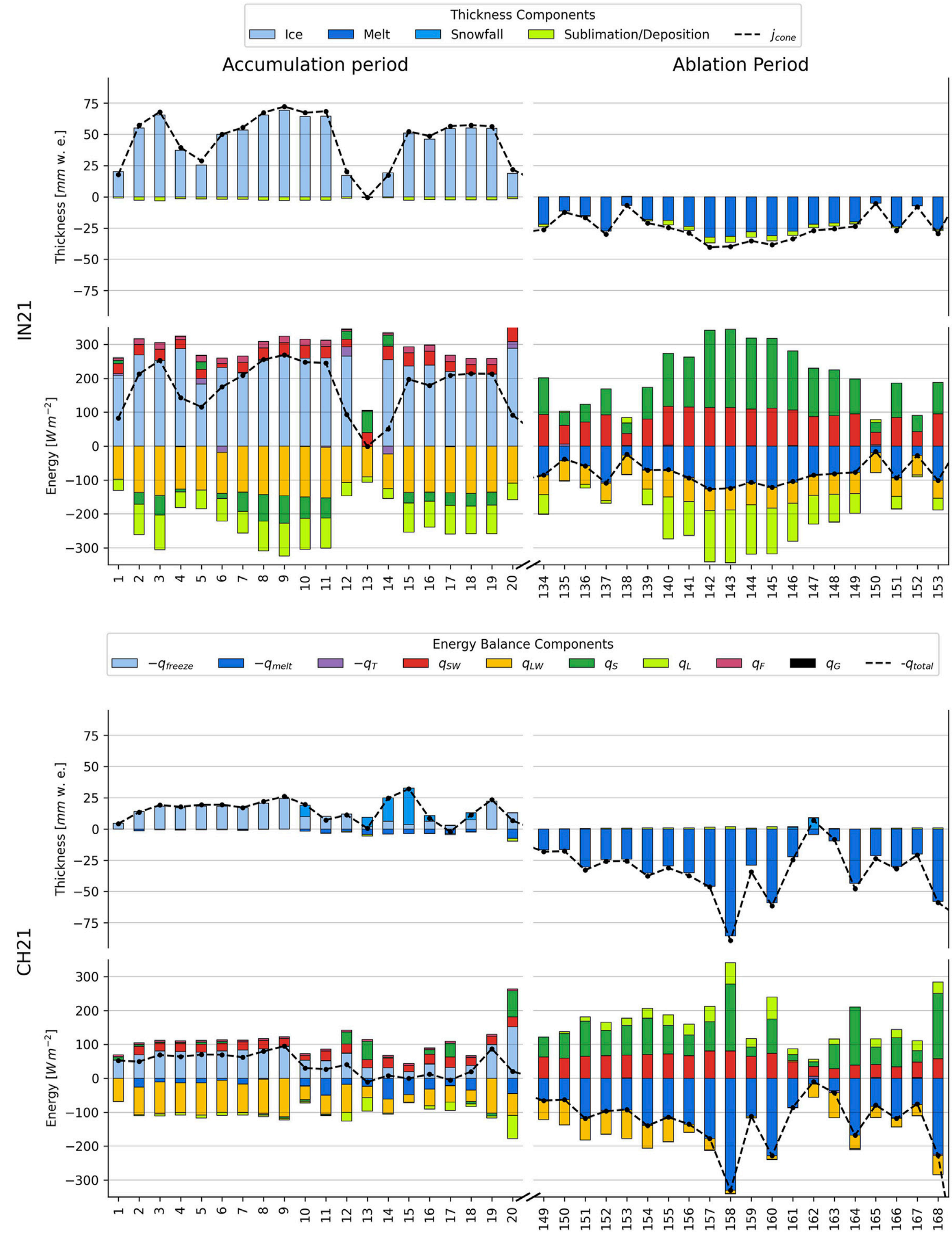

FIGURE 7 | Daily averages of thickness and energy balance components for the Indian and Swiss AIRs during the first 20 days of the accumulation and the last 20 days of the ablation period respectively.

AIR thickness growth was driven by the net radiation fluxes and the AIR thickness decay was driven by the net turbulent fluxes.

The longwave radiation flux had the highest energy turnover during the accumulation period for both locations. It increased and decreased the freezing and melting energy balance components during the accumulation and ablation period, respectively. However, its magnitude was much lower in the ablation period compared to the accumulation period since the rising air temperature increased the incoming longwave radiation in the ablation period. The mean longwave radiation flux (see **Table 4**) was lower for the Indian site as its incoming longwave radiation was strongly reduced due to cloud free skies. (see **Table 1**).

Global shortwave radiation was around two times higher for the Indian location due to its higher altitude and lower latitude. However, the energy turnover of the shortwave radiation for both sites were similar (see **Table 4**). The main cause of this is the differential exposure of a conical structure to direct and diffuse fractions of global shortwave radiation. This effect is quantified by the area fraction parameter f_{cone}. Less than 20 % of the AIR surface area on average was exposed to direct shortwave radiation flux for both locations. Cloudy days increase the diffuse fraction of global shortwave radiation. Therefore, the net shortwave radiation impact for the Indian site was significantly reduced as the study period had mostly clear days. Since the Swiss site had many cloudy days, its higher diffuse shortwave radiation enhanced the net shortwave radiation impact (see **Table 1**). Temporal variation in the f_{cone} factor due to increasing solar elevation angle and decreasing AIR slope leads to higher shortwave radiation in the ablation period compared to the accumulation period. Albedo, on the other hand, only varied temporally for the Swiss location because there was no precipitation for the Indian site.

Turbulent fluxes play an essential role in the energy balance. Sensible heat fluxes had the highest energy turnover during the ablation period for both locations. It decreased and increased the freezing and melting energy balance components respectively. The Indian location had a much higher sensible heat due to higher wind speeds and higher temperature gradient between the AIR surface and the atmosphere. The sensible heat contributes much more to the energy turnover during ablation period than the latent heat flux due to rising air temperature. Alternatively, latent heat flux does not vary much in energy turnover between the accumulation and ablation periods. For the Indian site, latent heat flux increased and decreased the freezing and melting energy, since sublimation was favoured throughout the simulation duration. On the contrary, for the Swiss location, latent heat increased both the freezing and the melting energy, as sublimation and deposition were favoured during the accumulation and ablation periods, respectively.

The mass contribution of the sublimation/deposition process (shown in **Table 5**) was significantly smaller than the energy flux contribution of this process (shown in **Table 4**), since the heat of vaporization is around nine times higher than the heat of fusion. The magnitude of the sublimation/deposition process was significantly different for both AIRs: IN21 AIR lost 2 % of its mass input to sublimation compared to the 1 % mass loss of CH21 AIR (see **Table 5**). For the IN21 AIR, the mass gain due to deposition was an order of magnitude smaller than the mass loss due to sublimation. For the CH21 AIR, there were no significant differences between the mass lost by sublimation and the mass gained by deposition. This was expected, since glaciers near the IN21 location have been hypothesized to lose a significant amount of their mass through sublimation, as suggested by Azam et al. (2018).

TABLE 4 | Contribution of the energy balance components (EBC) to the total energy turnover (the sum of energy fluxes in absolute values) during the accumulation and ablation periods with their daily mean (μ) and standard deviation (σ) for each site. The positive/negative sign is indicative of the upward/downward direction of the mean energy flux during the respective period.

	EBC	Accumulation	Ablation	$\mu \pm \sigma$
IN21	q_{SW}	16 %	25 %	$65 \pm 99\ W\,m^{-2}$
	q_{LW}	–43 %	–25 %	$-89 \pm 27\ W\,m^{-2}$
	q_S	13 %	30 %	$63 \pm 73\ W\,m^{-2}$
	q_L	–24 %	–20 %	$-63 \pm 62\ W\,m^{-2}$
	q_F	4 %	0 %	$4 \pm 7\ W\,m^{-2}$
	q_G	0%	0 %	$1 \pm 1\ W\,m^{-2}$
CH21	q_{SW}	21 %	23 %	$38 \pm 58\ W\,m^{-2}$
	q_{LW}	–41 %	–29 %	$-60 \pm 32\ W\,m^{-2}$
	q_S	23 %	39 %	$47 \pm 99\ W\,m^{-2}$
	q_L	–11 %	10 %	$-6 \pm 40\ W\,m^{-2}$
	q_F	3 %	0 %	$3 \pm 3\ W\,m^{-2}$
	q_G	0 %	0 %	$0 \pm 1\ W\,m^{-2}$

The fountain had some influence on the energy fluxes through its water temperature, temperature forcing and albedo forcing. However, this influence was insignificant compared to its influence on the surface area which was directly proportional to the fountain's spray radius during the accumulation period. Therefore, the thickness growth was uniformly scaled to produce the corresponding ice volume. Additionally, the higher spray radius of the Indian fountain resulted in a higher maximum ice volume. Nonetheless, this was accompanied by an earlier expiry date, as a larger surface area increased both the freezing and the melting rate.

5 DISCUSSION

5.1 Model Limitations

5.1.1 Fountain Quantification

The model requires the fountain spray radius to be provided as input. This is a significant limitation since the model is very sensitive to the spray radius parameter. Moreover, r_F is not only determined by the fountain characteristics but also due to refreezing and melting events across the AIR perimeter. Therefore, the same fountain may produce different spray radius under different weather conditions.

Contrary to our model assumptions, the parameters used to define the fountain were not independent. The fountain height, fountain aperture diameter (both ignored in this analysis), discharge rate, water temperature and spray radius were related through the trajectories of the water droplets. Particularly, the temporal variation of both the spray radius and the water temperature were completely ignored in the model. During the IN21 experiment, snow formation was observed, indicating that the fountain water droplets have the potential to freeze before deposition on the AIR surface. Modelling such processes would require modelling the conduction, convection and nucleation processes that all droplets undergo during their flight time. Therefore, a proper quantification of the fountain is

TABLE 5 | Summary of the mass balance and AIR characteristics estimated at the end of the respective simulation duration.

	Name	Symbol	IN21	CH21	Units
Input	Fountain discharge	M_F	2.90×10^6	9.70×10^5	*kg*
	Snowfall	M_{ppt}	0	5.60×10^4	*kg*
	Deposition	M_{dep}	6.30×10^3	4.10×10^3	*kg*
Output	Meltwater	M_{water}	2.40×10^5	2.30×10^5	*kg*
	Ice	M_{ice}	2.20×10^5	2.90×10^2	*kg*
	Sublimation	M_{sub}	4.80×10^4	5.20×10^3	*kg*
	Fountain wastewater	M_{waste}	2.50×10^6	8.00×10^5	*kg*
AIR	Freezing rate	$\Delta M_{freeze}/\Delta t$	11 ± 7	1 ± 2	*l*/min
	Melting rate	$\Delta M_{melt}/\Delta t$	2 ± 4	1 ± 2	*l*/min
	Thickness change	j_{cone}	3 ± 25	− 4 ± 27	*mm w. e.*
	Net Water Loss		81	77	%
	Maximum Ice Volume		685	155	m^3
	Surface Area	A_{cone}	350 ± 38	127 ± 34	m^2
Model	Surface layer thickness	Δx	65	45	*mm*
	RMSE with ice volume		41	10	m^3
	Correlation with ice volume		0.98	0.96	N.A.

much more complex and requires a closer look at the correlation of the fountain parameters amongst themselves and with the weather parameters. This will be investigated in a follow-up study, with this study focusing on the weather aspects of the model.

5.1.2 Shape Assumption

The RMSE between the drone and the model estimates of the surface area for the IN21, CH21 and CH20 AIRs were 69 %, 25 and 65 % of the maximum area of the respective AIRs (see **Table 2**). There are two crude assumptions that lead to such a large error namely, assuming a conical shape and assuming a constant spray radius.

Both these assumptions are a consequence of favoring model simplicity over accuracy. One could, for example, model the AIR shape assuming its cross section is a gaussian curve instead of a triangle. But such methodologies will involve the inclusion of even more model parameters.

5.2 Model Calibration, Validation and Uncertainty

The calibration process used has an inherent temporal and spatial bias due to the choice of when and how many drone surveys were possible in each location. Among the five surveys of IN21 AIR used for calibration, most of them were conducted around early March when the AIR volume was near its maximum whereas the seven surveys of the CH21 location were more evenly spaced out in comparison (see **Table 2**). Moreover, the fountain spray radius is also biased as a consequence leading to further model error. Overestimation of CH20 AIR's spray radius could be one of the reasons we observe an overestimation of its volume since the spray radius is derived from just one drone survey closer to the end of the accumulation period.

The calibration methodology assumed no correlation between the sensitive model hyperparameter Δx and the other eight parameters. Since for all AIRs, the total order sensitivity of Δx and the rest of the parameters was greater and lesser than 0.6 and 0.1, respectively, this was a reasonable assumption to make.

Theoretically, the parameter selection for Δx is based on the following two arguments: (a) the ice thickness Δx should be small enough to represent the surface temperature variations at every model time step Δt and (b) Δx should be large enough for these temperature variations to not reach the bottom of the surface layer. The minimum modelled ice and bulk temperatures decrease and increase with increasing Δx. Thus, we can reframe conditions (a) and (b) in terms of the relationship between T_{ice}, T_{bulk} and Δx. For example, all three AIRs studied had similar minimum modelled surface and bulk temperature around $-24\,^{\circ}C$ and $-3\,^{\circ}C$ respectively. Compared to T_{bulk}, the value of T_{ice} is not too high in accordance with (a) and not too low in accordance with (b). The magnitude of the difference expected between T_{ice} and T_{bulk} can be fixed with additional spatial and temporal ice temperature measurements of the AIR. This would lead to a better calibrated Δx. Therefore, uncertainty of the model could have been significantly reduced if such a temperature dataset had been available.

Practically, the surface layer thickness was also the only parameter compensating for the model's shape assumption. Since two AIRs merged to create the IN21 AIR, it had a drastically different shape evolution compared to the CH21 AIR. This also resulted in the different calibrated values of Δx in the Indian and the Swiss locations.

Uncertainty caused due to the other model parameters could also have been significantly reduced with further measurements. In particular, the fountain forcing parameters could have been avoided with a complete discharge rate dataset. Four out of the six uncertain weather parameters namely, α_{ice}, α_{snow}, τ and T_{ppt} could have been better constrained through periodic measurements with an albedometer and a snow height sensor.

The model results highlight the high water losses in all the chosen locations. This could have been verified independently if all AIR meltwater and wastewater had been stored in a tank. But there were two location-specific conditions that prevented us from doing so. First, the terrain of the site needs to be waterproof and oriented so that most of the AIR runoff can be collected. Second, the chosen location should not have high wind speeds, otherwise a significant fraction of AIR wastewater would be dispersed in the air. Both these conditions were not met for our chosen locations, hence efforts to measure the AIR runoff were abandoned. However, in an ideal location, this dataset could serve as a superior way to validate the model compared to the drone surveys which are also used for determining the spray radius.

5.3 Water Losses of AIRs

The net water losses of IN21 and CH21 AIR were 81 and 77 % of the total mass input, respectively. The high water losses were caused by the fountain wastewater for both AIRs. Therefore, AIRs lose water mostly during the accumulation period. The freezing rate of the IN21 AIR was less than 20 l min^{-1} for more than 90 % of the accumulation period, meaning that the growth was not limited by the water supply rate but rather by the freezing rate. The CH21 AIR freezing rate was able to reach the mean fountain discharge rate provided, albeit for only 2 h out of the 2155 h of fountain runtime available.

5.4 Fountain Optimization

Water losses could have been reduced in two ways: (a) reducing the fountain runtime t_F and (b) decreasing the mean fountain discharge rate d_F. For the CH21 AIR, strategy (a) could have saved considerable wastewater as no freezing was possible for 37 % of the accumulation period. For the IN21 site, strategy (b) would have yielded the least water loss as the freezing rate was more than half the mean discharge rate for just 2 hours . However, strategy (b) will also lead to a reduction in r_F if it is not accompanied by a suitable change in the fountain height and aperture diameter. So it can only be applied using the model if the corresponding fountain parameters are better parameterised.

Practically, both strategies are difficult to apply. It is unrealistic to expect someone constantly switching the fountain on and off under subzero conditions in accordance with strategy (a). Yes, strategy (b) is comparatively easier, but the minimum discharge rate is further constrained by the critical discharge rate below which the pipeline will freeze. However, both strategies can simultaneously be applied if the construction process is completely automated via a system that regulates the discharge in accordance with the model freezing estimates. Such a system can also drain the complete pipeline to prevent any pipeline freezing events. Since none of these functions are energy intensive, this system can be deployed anywhere using a solar powered energy source.

5.5 Favourable AIR Locations

Weather conditions play a significant role in making the Indian AIR larger and survive longer than the Swiss AIR, namely cloudiness, temperature and relative humidity. The lower cloudiness and mean winter temperature of the Indian location significantly reduced the net radiation flux during the accumulation period, enabling a faster AIR thickness growth. The lower winter temperature and humidity favour the sublimation over the deposition process, thus decreasing the magnitude of net turbulent fluxes during the ablation period. This results in a slower thickness decay. For AIRs with similar fountain parameters, we expect locations with lower cloudiness, lower mean winter temperature to augment freezing rates and locations with lower humidity to dampen melting rates. Hence, AIRs should be considered in the water resource management strategy particularly of dry and cold mountain regions such as in Central Asia or the Andes where few other sustainable and affordable alternatives exist.

5.6 Model Application in New Locations

Since the model has been validated in two drastically different weather conditions and uses a methodology similar to the ones used on glaciers worldwide, we believe it's performance should be similar in any other location.

The meteorological data and some fountain parameters are necessary to obtain modelled ice volume estimates. The necessary fountain parameters are r_F and t_F. The fountain runtime can be defined either with a fountain on and off date parameter or with a CSV file. Additionally, if d_F is known, the associated water losses can also be determined. As discussed before, the model is very sensitive to r_F, therefore it is recommended to manually measure the spray radius with the chosen fountain and pipeline.

All weather parameters can be assumed to have the median values of their ranges defined in **Table 3**. The model hyperparameter Δx needs to be calibrated beforehand. For a new location, we can use the surface layer thickness of CH21 AIR (45 mm) since it is representative of the shape evolution of a conical AIR.

The model is written in Python and completely based on open-source libraries. The model, source code, case studies and code examples for data preprocessing are provided on a freely accessible Git repository (https://github.com/Gayashiva/air_model, last access: December 17, 2021) for non-profit purposes. As a vision for the future, it is conceivable to extend the model for automatic AIR construction and foster a space where scientific and mountain communities can develop and apply various water resource management strategies together.

6 CONCLUSION

In this paper, we have developed a bulk energy and mass balance model to simulate AIR evolution using data from field measurements in Gangles, India and Guttannen, Switzerland. The use of these datasets, in combination with the novel model, allowed for an accurate representation of the complex evolution that is typical of an AIR. The model was calibrated and validated with ice volume and surface area observations obtained via drone surveys. We calculated the freezing and melting rates for each of the three AIRs and explained their corresponding magnitudes in terms of the influence of the chosen location and the fountain used. Our main conclusions are summarized below:

- The model was successful in reproducing the observed ice volume evolution with a correlation greater than 0.96 and an RMSE less than 18 % of the maximum ice volume for all AIRs.
- The ice volume achieved after the accumulation period was much higher for the Indian AIR compared to the Swiss AIRs. The lower net radiation fluxes of the Indian location favored a

faster thickness growth and the spray radius of the Indian fountain produced a higher surface area compared to the Swiss counterparts. Thus, the more than three times higher mean surface area and four times higher mean thickness growth during the two times shorter accumulation period of the Indian location resulted in a four times higher maximum ice volume of the Indian AIR compared to the Swiss.

- The ablation period of the Indian AIR was longer than the Swiss AIRs. However, the lower turbulent fluxes resulted in a slower thickness decay on a larger surface area. This rendered the differences between the IN21 and CH21 melting rates negligible. Since the accumulation period produced much higher ice volumes, the Indian AIR was able to last much longer than the Swiss AIRs.
- Water losses were high (> 77 %) mostly due to fountain wastewater for all AIRs. Vapour losses were insignificant (< 2 %) in comparison. However, a significant reduction in water loss is possible through optimization of fountain discharge rate.
- The Indian construction site produced long-lasting AIRs with higher maximum ice volumes since it was colder, drier and less cloudy compared to the Swiss construction site. Thus, the AIR technology is ideally suited to serve as a water management strategy, especially in dry and cold mountain regions such as in Central Asia or the Andes impacted by climate change induced water stress.

DATA AVAILABILITY STATEMENT

Model code is freely available on GitHub (https://github.com/Gayashiva/air_model, last access: 17 December 2021) for non-profit purposes. The drone data can be obtained from the authors upon request.

AUTHOR CONTRIBUTIONS

SB, MH, SW, and FK designed the study. SB developed the methodology with inputs from MH. MH, ML, and JO reviewed the algorithm and helped improve it. SB processed the drone data. SB wrote the model code. JB helped with model validation and uncertainty assessment. SB, MH, FK, and SW participated in the fieldwork. SB led the writing of the paper and all co-authors contributed to it.

FUNDING

This work was supported and funded by the University of Fribourg and by the Swiss Government Excellence Scholarship (SB). The associated fieldwork in India was supported by the Himalayan Institute of Alternatives and funded by the Swiss Polar Institute.

ACKNOWLEDGMENTS

This work would not have been possible without the untiring efforts of the Swiss and Indian icestupa construction teams through the winters of 2019, 2020, and 2021. We thank Mr. Adolf Kaeser and Mr. Flavio Catillaz from Eispalast Schwarzsee (CH19); Daniel Bürki from the Guttannen Bewegt Association (CH20 and CH21); Norboo Thinles, Nishant Tiku, Sourabh Maheshwari and the rest of the HIAL team (IN21). We would also like to thank Hansueli Gubler for designing the Swiss AWS; Dr. Tom Matthews for designing the Indian AWS; Michelle Stirnimann for conducting the CH20 drone surveys and Digmesa AG for subsidising their flowmeter used in the experiment. We would particularly like to thank Prof. Thomas Schuler and 4 reviewers who gave us important inputs to improve the paper. We also thank Prof. Christian Hauck, Prof. Nanna B. Karlsson Dr. Andrew Tedstone and Alizé Carrère for valuable suggestions that improved the manuscript.

SUPPLEMENTARY MATERIAL

The Supplementary Material for this article can be found online at: https://www.frontiersin.org/articles/10.3389/feart.2021.771342/full#supplementary-material

REFERENCES

Apel, H., Abdykerimova, Z., Agalhanova, M., Baimaganbetov, A., Gavrilenko, N., Gerlitz, L., et al. (2018). Statistical Forecast of Seasonal Discharge in central Asia Using Observational Records: Development of a Generic Linear Modelling Tool for Operational Water Resource Management. *Hydrol. Earth Syst. Sci.* 22, 2225–2254. doi:10.5194/hess-22-2225-2018

Azam, M. F., Wagnon, P., Berthier, E., Vincent, C., Fujita, K., and Kargel, J. S. (2018). Review of the Status and Mass Changes of Himalayan-Karakoram Glaciers. *J. Glaciol.* 64, 61–74. doi:10.1017/jog.2017.86

Bonales, L. J., Rodriguez, A. C., and Sanz, P. D. (2017). Thermal Conductivity of Ice Prepared under Different Conditions. *Int. J. Food Properties* 20, 610–619. doi:10.1080/10942912.2017.1306551

Brock, B. W., Willis, I. C., and Sharp, M. J. (2006). Measurement and Parameterization of Aerodynamic Roughness Length Variations at Haut Glacier d'Arolla, Switzerland. *J. Glaciol.* 52, 281–297. doi:10.3189/172756506781828746

Brutsaert, W. (1982). *Evaporation into the Atmosphere. Theory, History and Application*. Kluwer Academic Publishers.

Brutsaert, W. (1975). On a Derivable Formula for Long-Wave Radiation from clear Skies. *Water Resour. Res.* 11, 742–744. doi:10.1029/WR011i005p00742

Buytaert, W., Moulds, S., Acosta, L., De Bièvre, B., Olmos, C., Villacis, M., et al. (2017). Glacial Melt Content of Water Use in the Tropical andes. *Environ. Res. Lett.* 12, 114014. doi:10.1088/1748-9326/aa926c

Chen, Y., Li, W., Deng, H., Fang, G., and Li, Z. (2016). Changes in central Asia's Water tower: Past, Present and Future. *Nature* 6, 35458. doi:10.1088/1748-9326/aa926c

[Dataset] Copernicus Climate Change Service (C3S) (2017). Era5: Fifth Generation of Ecmwf Atmospheric Reanalyses of the Global Climate. Available at https://cds.climate.copernicus.eu/cdsapp#!/home (Accessed 10 01, 2019).

Cuffey, K. M., and Paterson, W. S. B. (2010). *The Physics of Glaciers*. Elsevier.

Furukawa, Y., and Ponce, J. (2010). Accurate, Dense, and Robust Multiview Stereopsis. *IEEE Trans. Pattern Anal. Mach. Intell.* 32, 1362–1376. doi:10.1109/TPAMI.2009.161

Garratt, J. R. (1992). *The Atmospheric Boundary Layer*. Cambridge University Press.

Grossman, D. (2015). As Himalayan Glaciers Melt, Two Towns Face the Fallout. Available at https://e360.yale.edu/features/as_himalayan_glaciers_melt_two_towns_face_the_fallout (Accessed 10 01, 2019).

Hock, R., Rasul, G., Adler, C., Cáceres, B., Gruber, S., Hirabayashi, Y., et al. (2019). "2019: High Mountain Areas," in *IPCC Special Report on the Ocean and Cryosphere in a Changing Climate*. Editors H.-O. Pörtner, D. C. Roberts, V. Masson-Delmotte, P. Zhai, M. Tignor, E. Poloczanska, et al. (Cambridge, United Kingdom: Cambridge University Press).

Hoelzle, M., Barandun, M., Bolch, T., Fiddes, J., Gafurov, A., Muccione, V., et al. (2019). The Status and Role of the alpine Cryosphere in Central Asia, 100, 121. doi:10.4324/9780429436475-8

Hori, M., Aoki, T., Tanikawa, T., Motoyoshi, H., Hachikubo, A., Sugiura, K., et al. (2006). *In-situ* Measured Spectral Directional Emissivity of Snow and Ice in the 8-14 µm Atmospheric Window. *Remote Sensing Environ.* 100, 486–502. doi:10.1016/j.rse.2005.11.001

Huang, J. (2018). A Simple Accurate Formula for Calculating Saturation Vapor Pressure of Water and Ice. *AMETSOC* 57, 1265–1272. doi:10.1175/JAMC-D-17-0334.1

Immerzeel, W. W., Lutz, A. F., Andrade, M., Bahl, A., Biemans, H., Bolch, T., et al. (2019). Importance and Vulnerability of the World's Water Towers. *Nature* 577, 364–369. doi:10.1038/s41586-019-1822-y

Küng, O., Strecha, C., Beyeler, A., Zufferey, J.-C., Floreano, D., Fua, P., et al. (2011). The Accuracy of Automatic Photogrammetric Techniques on Ultra-light Uav Imagery. *Int. Arch. Photogramm. Remote Sens. Spat. Inf. Sci.* XXXVIII-1/C22, 125–130. doi:10.5194/isprsarchives-XXXVIII-1-C22-125-2011

Labbal, V. (2000). *Traditional Oases of Ladakh: A Case Study of Equity in Water Management*. Oxford, UK: Oxford University Press, 163–183.

Lowe, D. G. (2004). Distinctive Image Features from Scale-Invariant Keypoints. *Int. J. Comp. Vis.* 60, 91–110. doi:10.1023/B:VISI.0000029664.99615.94

Meteoblue (2021). Climate Guttannen. Available at https://www.meteoblue.com/en/weather/historyclimate/climatemodelled/guttannen_switzerland_2660433 (Accessed 07 19, 2021).

Mölg, N., and Bolch, T. (2017). Structure-from-motion Using Historical Aerial Images to Analyse Changes in Glacier Surface Elevation. *Remote Sensing* 9, 1021. doi:10.3390/rs9101021

Mölg, T., and Hardy, D. R. (2004). Ablation and Associated Energy Balance of a Horizontal Glacier Surface on Kilimanjaro. *J. Geophys. Res.* 109, 1–13. doi:10.1029/2003JD004338

Nüsser, M., Dame, J., Kraus, B., Baghel, R., and Schmidt, S. (2019a). Socio-hydrology of "artificial Glaciers" in Ladakh, India: Assessing Adaptive Strategies in a Changing Cryosphere. *Reg. Environ. Change* 19, 1327–1337. doi:10.1007/s10113-018-1372-0

Nüsser, M., Dame, J., Parveen, S., Kraus, B., Baghel, R., and Schmidt, S. (2019b). Cryosphere-Fed Irrigation Networks in the Northwestern Himalaya: Precarious Livelihoods and Adaptation Strategies under the Impact of Climate Change. *Mountain Res. Dev.* 39. doi:10.1659/MRD-JOURNAL-D-18-00072.1

Nüsser, M., Schmidt, S., and Dame, J. (2012). Irrigation and Development in the Upper Indus Basin: Characteristics and Recent Changes of a Socio-Hydrological System in Central Ladakh, India. *Mountain Res. Dev.* 32, 51–61. doi:10.1659/MRD-JOURNAL-D-11-00091.1

Oerlemans, J., Balasubramanian, S., Clavuot, C., and Keller, F. (2021). Brief Communication: Growth and Decay of an Ice Stupa in alpine Conditions - a Simple Model Driven by Energy-Flux Observations over a Glacier Surface. *The Cryosphere* 15, 3007–3012. doi:10.5194/tc-15-3007-2021

Oerlemans, J., and Knap, W. H. (1998). A 1 Year Record of Global Radiation and Albedo in the Ablation Zone of Morteratschgletscher, switzerland. *J. Glaciol.* 44, 231–238. doi:10.3189/S0022143000002574 10.1017/s0022143000002574

Sa, P. (2020). Pix4dmapper 4.1 User Manual. Available at https://support.pix4d.com/hc/en-us/articles/204272989-Offline-Getting-Started-and-Manual-pdf (Accessed 12 09, 2021).

Scherrer, S. C. (2020). Temperature Monitoring in Mountain Regions Using Reanalyses: Lessons from the Alps. *Environ. Res. Lett.* 15, 044005. doi:10.1088/1748-9326/ab702d

Schmidt, L. S., Aðalgeirsdóttir, G., Guðmundsson, S., Langen, P. L., Pálsson, F., Mottram, R., et al. (2017). The Importance of Accurate Glacier Albedo for Estimates of Surface Mass Balance on Vatnajökull: Evaluating the Surface Energy Budget in a Regional Climate Model with Automatic Weather Station Observations. *The Cryosphere* 11, 1665–1684. doi:10.5194/tc-11-1665-2017

Schmidt, S., and Nüsser, M. (2012). Changes of High Altitude Glaciers from 1969 to 2010 in the Trans-himalayan Kang Yatze Massif, Ladakh, Northwest india. *Arctic, Antarctic, Alpine Res.* 44, 107–121. doi:10.1657/1938-4246-44.1.107

Steiner, J. F., Pellicciotti, F., Buri, P., Miles, E. S., Immerzeel, W. W., and Reid, T. D. (2015). Modelling Ice-Cliff Backwasting on a Debris-Covered Glacier in the Nepalese Himalaya. *J. Glaciol.* 61, 889–907. doi:10.3189/2015JoG14J194

Tennøe, S., Halnes, G., and Einevoll, G. T. (2018). Uncertainpy: A python Toolbox for Uncertainty Quantification and Sensitivity Analysis in Computational Neuroscience. *Front. Neuroinform.* 12, 49. doi:10.3389/fninf.2018.00049

Thayyen, R. J., and Gergan, J. T. (2010). Role of Glaciers in Watershed Hydrology: a Preliminary Study of a "Himalayan Catchment". *The Cryosphere* 4, 115–128. doi:10.5194/tc-4-115-2010

Turner, D., Lucieer, A., and Watson, C. (2012). An Automated Technique for Generating Georectified Mosaics from Ultra-high Resolution Unmanned Aerial Vehicle (Uav) Imagery, Based on Structure from Motion (Sfm) point Clouds. *Remote Sensing* 4, 1392–1410. doi:10.3390/rs4051392

Unger-Shayesteh, K., Vorogushyn, S., Farinotti, D., Gafurov, A., Duethmann, D., Mandychev, A., et al. (2013). What Do We Know about Past Changes in the Water Cycle of central Asian Headwaters? a Review. *Glob. Planet. Change* 110, 4–25. doi:10.1016/j.gloplacha.2013.02.004

Wangchuk, S. (2015b). Ice Stupa Artificial Glacier Inaugurated. Available at http://icestupa.org/news/ice-stupa-artificial-glacier-inaugurated-5th-of-march (Accessed 10 01, 2019).

Wangchuk, S. (2014). Ice Stupa Artificial Glaciers of Ladakh. Available at www.indiegogo.com/projects/ice-stupa-artificial-glaciers-of-ladakh#/(Accessed 10 01, 2019).

Wangchuk, S. (2021). Ice Stupa Competition. Available at https://tribal.nic.in/IceStupa.aspx (Accessed 12 13, 2021).

Wangchuk, S. (2015c). Ice Stupa Surpasses Guiness World Record. Available at http://icestupa.org/news/ice-stupa-surpasses-guinness-world-record (Accessed 10 01, 2019).

Wangchuk, S. (2015d). Ice Stupa Way of Celebrating a Special Day. Available at http://icestupa.org/news/ice-stupa-way-of-celebrating-a-special-day6th-of-ju (Accessed 10 01, 2019).

Wangchuk, S. (2015a). The Good News at Ice Stupa. Available at http://icestupa.org/news/the-good-news-at-ice-stupa (Accessed 10 01, 2019).

Wangchuk, S. (2015e). World Water Day at Ice Stupa. Available at http://icestupa.org/news/world-water-day-at-ice-stupa (Accessed 10 01, 2019).

Woolf, H. M. (1968). *On the Computation of Solar Elevation Angles and the Determination of Sunrise and sunset Times*. Washington, DC: National Aeronautics and Space Administration. Available at https://ntrs.nasa.gov/citations/19680025707 (Accessed April 01, 2022).

Xiu, D., and Hesthaven, J. S. (2005). High-order Collocation Methods for Differential Equations with Random Inputs. *SIAM J. Sci. Comput.* 27, 1118–1139. doi:10.1137/040615201

Zhou, S., Kang, S., Gao, T., and Zhang, G. (2010). Response of Zhadang Glacier Runoff in Nam Co basin, Tibet, to Changes in Air Temperature and Precipitation Form. *Chin. Sci. Bull.* 55, 2103–2110. doi:10.1007/s11434-010-3290-5

Zolles, T., Maussion, F., Galos, S. P., Gurgiser, W., and Nicholson, L. (2019). Robust Uncertainty Assessment of the Spatio-Temporal Transferability of Glacier Mass and Energy Balance Models. *The Cryosphere* 13, 469–489. doi:10.5194/tc-13-469-2019

Conflict of Interest: The authors declare that the research was conducted in the absence of any commercial or financial relationships that could be construed as a potential conflict of interest.

Symbols

a	distance	m
P	power	W (Js^{-1})
ω	angular frequency	$rads^{-1}$

List of Figures

List of Tables

Abbreviations

AIR	**A**rtificial **I**ce **R**eservoirs
SIR	**S**easonal **I**ce **R**eservoirs
PIR	**P**erpetual **I**ce **R**eservoirs
HIR	**H**orizontal **I**ce **R**eservoirs
VIR	**V**ertical **I**ce **R**eservoirs

Physical Constants

Speed of Light $c = 2.997\ 924\ 58 \times 10^{8}\ \mathrm{ms^{-S}}$ (exact)

Acknowledgements

The acknowledgements and the people to thank go here, don't forget to include your project advisor…

Bibliography

[1] Biswajit Mukhopadhyay and Asif Khan. A reevaluation of the snowmelt and glacial melt in river flows within Upper Indus Basin and its significance in a changing climate. *Journal of Hydrology*, 527:119–132, August 2015. ISSN 0022-1694. doi: 10.1016/j.jhydrol.2015.04.045.

[2] Marcus Nüsser and Ravi Baghel. Local Knowledge and Global Concerns: Artificial Glaciers as a Focus of Environmental Knowledge and Development Interventions. In Peter Meusburger, Tim Freytag, and Laura Suarsana, editors, *Ethnic and Cultural Dimensions of Knowledge*, Knowledge and Space, pages 191–209. Springer International Publishing, Cham, 2016. ISBN 978-3-319-21900-4. doi: 10.1007/978-3-319-21900-4_9.

[3] Chewang Norphel and Padma Tashi. Snow Water Harvesting in the Cold Desert in Ladakh: An Introduction to Artificial Glacier. In Hari Krishna Nibanupudi and Rajib Shaw, editors, *Mountain Hazards and Disaster Risk Reduction*, Disaster Risk Reduction, pages 199–210. Springer Japan, Tokyo, 2015. ISBN 978-4-431-55242-0. doi: 10.1007/978-4-431-55242-0_11.

[4] Pallava Bagla. Artificial Glaciers to Help Farmers. *Science*, 282(5389):619–619, October 1998. doi: 10.1126/science.282.5389.619a.

[5] Carey Clouse, Naomi Anderson, and Taylor Shippling. Ladakh's artificial glaciers: Climate-adaptive design for water scarcity. *Climate and Development*, 9(5):428–438, 2017. doi: 10.1080/17565529.2016.1167664.

[6] Meteoblue. Climate Guttannen. https://www.meteoblue.com/en/weather/historyclimate/climaten February 2021.

[7] Marcus Nüsser, Susanne Schmidt, and Juliane Dame. Irrigation and Development in the Upper Indus Basin: Characteristics and Recent Changes of a Socio-hydrological System in Central Ladakh, India. *Mountain Research and Development*, 32(1):51–61, 2012. doi: 10.1659/MRD-JOURNAL-D-11-00091.1.

[8] Kurt M. Cuffey and W. S. B. Paterson. *The Physics Of Glaciers*. Elsevier, 2010.

[9] J. Oerlemans and W. H. Knap. A 1 year record of global radiation and albedo in the ablation zone of Morteratschgletscher, Switzerland. *Journal of Glaciology*, 44 (147):231–238, 1998. doi: 10.3189/S0022143000002574.

[10] Harold M. Woolf. *On the Computation of Solar Elevation Angles and the Determination of Sunrise and Sunset Times*. National Aeronautics and Space Administration, 1968.

[11] W. Brutsaert. *Evaporation into the Atmosphere. Theory, History and Application*. Kluwer Academic Publishers, 1982.

[12] W. Brutsaert. On a derivable formula for long-wave radiation from clear skies. *Water Resources Research*, 11(1-4):742–744, 1975. doi: 10.1029/WR011i005p00742.

[13] J. R. Garratt. *The Atmospheric Boundary Layer*. Cambridge University Press, 1992.

[14] Jianhua Huang. A Simple Accurate Formula for Calculating Saturation Vapor Pressure of Water and Ice. *AMETSOC*, 57, June 2018. doi: 10.1175/JAMC-D-17-0334.1.

[15] J. Oerlemans, S. Balasubramanian, C. Clavuot, and F. Keller. Brief communication: Growth and decay of an ice stupa in alpine conditions – a simple model driven by energy-flux observations over a glacier surface. *The Cryosphere*, 15(6):3007–3012, 2021. doi: 10.5194/tc-15-3007-2021.

[16] Chewang Norphel. Artificial glacier: A high altitude cold desert water conservation technique. (Energy and Climate Change in cold regions of Asia: Proccedings of the Seminar, Ladakh, India):62–64, 2009.

[17] Gaia Vince. Glacier Man. *Science*, 326(5953):659–661, October 2009. doi: 10.1126/science.326_659.